



Supported PdZn nanoparticles for selective CO₂ conversion, through the grafting of a heterobimetallic complex on CeZrO_x

Paolo Ruzzi, Davide Salusso, Matilde Baravaglio, Kai Szeto, Aimery De mallmann, Laia Gil Jiménez, Cyril Godard, Anass Benayad, Sara Morandi, Silvia Bordiga, et al.

► To cite this version:

Paolo Ruzzi, Davide Salusso, Matilde Baravaglio, Kai Szeto, Aimery De mallmann, et al.. Supported PdZn nanoparticles for selective CO₂ conversion, through the grafting of a heterobimetallic complex on CeZrO_x. *Applied Catalysis A: General*, 2022, 635, pp.118568. 10.1016/j.apcata.2022.118568 . hal-03759556

HAL Id: hal-03759556

<https://hal.science/hal-03759556>

Submitted on 24 Aug 2022

HAL is a multi-disciplinary open access archive for the deposit and dissemination of scientific research documents, whether they are published or not. The documents may come from teaching and research institutions in France or abroad, or from public or private research centers.

L'archive ouverte pluridisciplinaire **HAL**, est destinée au dépôt et à la diffusion de documents scientifiques de niveau recherche, publiés ou non, émanant des établissements d'enseignement et de recherche français ou étrangers, des laboratoires publics ou privés.

Supported PdZn nanoparticles for selective CO₂ conversion, through the grafting of a heterobimetallic complex on CeZrO_x

Ruzzi Paolo^a, Salusso Davide^b, Baravaglio Matilde^{a,b}, Szeto Kai C^a, De Mallmann Aimery^a, Laia Gil Jiménez,^c Godard Cyril,^c Benayad Anass^d, Morandi Sara^b, Bordiga Silvia^{b*}, Taoufik Mostafa^{a*}

*corresponding authors

^a Université de Lyon 1, CPE Lyon, CNRS-UMR 5128 – laboratoire Catalyse, Polymérisation, Procédés et Matériaux (CP2M), F-69616 Villeurbanne, France. Email: mostafa.taoufik@univ-lyon1.fr

^b Department of Chemistry, NIS Center and INSTM Reference Center, University of Turin, 10125, Turin, Italy. Email: silvia.bordiga@unito.it

^c Departament de Química Física i Inorgànica, Universitat Rovira i Virgili, Marcel·lí Domingo s/n, Campus Sescelades, 43007 Tarragona, Spain,

^d Université Grenoble Alpes, CEA-LITEN, 17 rue des Martyrs, 38054 Grenoble Cedex 9, France

Abstract

Controlling the stoichiometry of supported bimetallic nanoparticles is essential in many catalytic reactions, notably selective CO₂ hydrogenation. Thus, a new strategy to ensure the preferred stoichiometry (1:1) of supported bimetallic PdZn nanoparticles is presented, involving the deposition of a heterobimetallic precursor, [PdZn(μ-OOCMe)₄]₂ on a CeZrO_x support. After calcination and reduction, the material contained mainly a PdZn alloy, as revealed by powder XRD and XAFS, and further supported by XPS, TEM-EDX, elemental analysis and in-situ IR at low temperature using CO as probe molecule. Moreover, a minor phase of oxidized Zn was determined by XAFS. This PdZn/CeZrO_x reduced catalyst was combined with SAPO-34 to form a tandem catalytic system for CO₂ conversion to hydrocarbons. This system could readily convert CO₂ and H₂ at high temperature (380 °C) into hydrocarbons with a conversion of 24% and high relative selectivity in light hydrocarbons (C₂-C₃: 82%) with virtually no deactivation of the catalyst after 16 hours on stream. Controlled experiments were performed with Pd/CeZrO_x and Zn/CeZrO_x in order to gain supplementary insights on this system: Pd/CeZrO_x gave only methane and Zn/CeZrO_x gave mainly CO under the same conditions. The latter clearly shows that the control of the formation of PdZn phase has great impact for the selective production of hydrocarbons.

Keywords: surface organometallic chemistry, in-situ IR, hydrocarbon production, palladium, light alkanes

1. Introduction

Constant increase of the CO₂ concentration in the atmosphere has resulted in environmental changes such as global warming and ocean acidification [1–5]. Any action to decrease the CO₂ emission or concentration in the atmosphere is of great interest. Among them are carbon capture and storage (CCS), and carbon capture and utilization (CCU) [6,7]. CCU seems to be more valuable and sustainable than CCS [8,9]. Although CO₂ seems to be an undesired molecule, it can theoretically be served as an inexpensive, non-toxic, non-flammable and sustainable carbon source to produce high value products such as fuels and chemicals [10,11]. However, due to its high stability, CO₂ has to be activated by heat, light, or electricity (thermochemical, photochemical, electrochemical, or photo-electrochemical processes)[12–16], and more efficiently assisted by a catalyst. Nowadays, the processes based on thermo-catalytic conversion of CO₂ show suitable productivity at commercial scale. Indeed, these processes lead to a variety of carbon-based products, including carbon monoxide, formaldehyde, methanol, methane, or light hydrocarbons (e.g., ethylene, propylene) [17,18], depending on the nature of the catalyst. Chemical conversion of CO₂ to value-added chemicals and fuels potentially presents an important supply for the declining and non-renewable fossil fuels that are currently the major source of chemicals and energy being inevitable in current society [19,20].

Transformation of CO₂ into hydrocarbon-based fuels can be achieved via hydrogenation through two different ways: i) synthesis gas production by the reverse water-gas shift (RWGS) reaction followed by Fischer-Tropsch (FT) reaction to produce hydrocarbons [21]; ii) methanol synthesis [22] accompanied by methanol-to-olefin (MTO) process [23,24]. The second method is more selective and lead to C₂-C₄ olefins while FT synthesis leads to a Schultz-Flory-Anderson distribution of hydrocarbons that needs to be treated by cracking and separation in order to obtain the desired products [25]. Moreover, CO₂ hydrogenation via methanol requires lower energy and cost than the other route. Consequently, the cascade reaction to produce light hydrocarbons through methanol has motivated many research groups for extensive exploration. Obviously, this process requires two different catalysts, first for the conversion of CO₂ into methanol intermediate, supported metal nanoparticles or metal oxide or mixed oxide (e.g. In₂O₃, ZnO, ZrO₂/ZnO) catalysts can be used. Second, MTO reaction can be readily catalyzed by zeolites, such as ZSM-5 or SAPO-34 [26–28].

The main challenge of catalytic CO₂ hydrogenation into hydrocarbons over a single reactor is the presence of the RWGS reaction, which is kinetically favored leading to the production of CO. Particularly at high working temperatures required for MTO (over 350 °C), the selectivity of CO can be over 80%. Moreover, water formed during CO₂ hydrogenation to hydrocarbons using bifunctional catalysts can alter the activity and stability of the zeolite. Therefore, synthesis of light hydrocarbons with a high selectivity from CO₂ hydrogenation over a bifunctional catalyst is very challenging. Despite some promising results, the aforementioned issues, like high CO selectivity, frequently higher than 50% and the proper zeolite selection still have to be overcome. Furthermore, the hydrogenation of CO₂ is thermodynamically unfavorable, but the conversion of methanol to lower olefins is considerably favorable. Hence, a cascade process by coupling these two reactions gives an additional driving force to convert the formed methanol and thereby make the overall process (CO₂ to light hydrocarbons) feasible. However, this thermodynamic coupling is observed only when the two catalytic components are in intimate contact [29,30].

Several tandem catalytic systems are reported in the literature. For example, ZnO-ZrO₂ mixed with Zn-modified SAPO-34 shows high relative selectivity (among hydrocarbons) towards lower olefins (80–90%) but accompanied with a high selectivity in undesired CO (ca. around 50%). Surprisingly, the CO selectivity for the tandem catalysts is already significantly suppressed compared to the ZnO-ZrO₂ mixed oxide alone [31]. The reason is probably associated to the formation of water by the MTO reaction catalyzed by the zeolite that will trigger the water-gas shift reaction, resulting in the consumption of CO. Another aspect to limit the formation of CO is to select a proper active phase in order to minimize the RWGS reaction upon hydrogenation of CO₂ to hydrocarbons under the given working temperature (over 350 °C). Based on thermodynamic and kinetic analyses of this process (CO₂ to hydrocarbon via methanol) along with literature reports, the greatest challenge lies on the methanol synthesis catalyst. Several metals, metal alloys and metal oxides were used for CO₂ hydrogenation to MeOH, including catalysts based on other mixed oxides, for example In₂O₃/ZrO₂ [30,31] or ZnO/ZrO₂ [32–37] or noble metal such as supported Pd-NPs, PdZn-based catalysts have shown promising MeOH yield especially at medium temperatures (210–270 °C) [38–43]. Supplementary screening of different catalysts with various compositions revealed that the methanol production can be enhanced by increasing the Zn/Pd ratio [39,40]. The latter is attributed to increased Zn⁽⁰⁾ incorporation in the Pd lattice, ensuring the formation of surface PdZn (1:1 ratio) alloy which is believed to be the most important phase for methanol production. Complementary experiments conducted on Pd (without Zn) supported on TiO₂ or Al₂O₃ showed that CO was the predominant product, indicating that Pd nanoparticles promote the RWGS reaction. A mechanistic study using DRIFT and DFT calculations proposed two possible intermediates in CO₂ hydrogenation over PdZn catalysts: (i) HCOO which directly hydrogenates to

MeOH or (ii) trans-COOH, which isomerize to cis-COOH for RWGS reaction or MeOH [39–42]. Trans-COOH formation was found to be energetically favored on pure Pd (111) while it was highly unstable on Pd₁Zn₁ (111). These findings are in good agreement with experimental data, and highlight the importance of the PdZn (1:1) alloy for hydrogenation of CO₂ to methanol. Furthermore, different supports were also studied. Apart from the robust ZrO₂ support, the presence of Cerium seems to have a beneficial effect due to supplementary CO₂ uptake [44,45]. Since the ultimate goal is to produce light hydrocarbons from CO₂, additional circumstances, such as thermodynamic and the involvement of MTO catalyst, have to be considered. Methanol formation is generally favored at fairly low temperatures (around 250 °C). At higher temperature, production of CO becomes favorable. Unfortunately, the MTO reaction requires higher temperature (> 350 °C) to be efficient. Hence, an expected challenge will be to minimize the CO selectivity. In addition, a recent study of the PdZn system mechanically mixed with H-ZSM-5 and PdZn on meso-porous H-ZSM-5 (prepared through surface organometallic chemistry on metal) revealed that Zn has a tendency to exchange with Brønsted proton. During the catalytic process, this resulted in an inhibition of the hydrocarbon production [46]. Gathering information from the literature for Pd-based methanol synthesis catalysts, an enhanced system should contain PdZn alloy having the preferred stoichiometry (1:1). Moreover, employing a Ce-based support is favorable in order to maximize the CO₂ uptake. Hence, we hereby describe a methodology to access such system by applying surface organometallic chemistry with a heterobimetallic precursor based on Pd and Zn onto a commercial ceria-zirconia support. We also prepared PdZn alloy onto pure ZrO₂ to directly compare SOMC to the same catalyst prepared by colloidal impregnation recently applied to prepare PdZn/ZrO₂ catalyst [47]. Employing a heterobimetallic precursor will ensure the desired stoichiometry between Pd and Zn (1:1), which is essential for this system and has already shown to enhance the catalytic activity for partial acetylene hydrogenation [48]. Furthermore, the surface organometallic chemistry approach involves grafting of the selected precursor onto the support, offering a firmly bonded intermediate and thereby minimizing migration and leaching of the elements upon calcination and reduction. In addition, this synthesis strategy will avoid formation of local monometallic nanoparticles or clusters that may occur by using conventional preparation methods like wetness impregnation and sol-gel synthesis. In this paper, we report the synthesis of PdZn nanoparticles supported on ceria-zirconia and the characterization of the material by elemental analysis, Surface and porosity analyses, IR, PXRD, TEM and EDX, CO adsorption followed by IR, XPS, and EXAFS. The catalytic performance in the conversion of CO₂ of the different tandem catalysts composed of supported PdZn mechanically mixed with commercial SAPO-34 are reported. For comparison complementary catalysts containing PdZn supported on ceria and on zirconia and monometallic Pd and Zn supported ceria-zirconia were also prepared to gain further

comprehension. Finally, the most promising system, being PdZn/CeZrOx was characterized by XAS and in-situ IR.

2. Experimental

2.1 Catalysts preparation

Commercial Ceria (Solvay ACTALYS HSA 5) and Ceria Zirconia (Solvay ACTALYS 922, CeZrOx with a CeO₂/ZrO₂ ratio of 58-42 %wt) were purchased from Solvay. Zirconia was synthesized from Zr(IV) hydroxide (Sigma-Aldrich, CAS number 14475-63-9) by calcination in a dry oxygen flow at 500 °C for 16 h.

Ceria, Zirconia and Ceria Zirconia were calcined for 16 h at 500 °C under a flow of dry air, then cooled down under vacuum. After a re-hydration under an inert atmosphere, the oxides were partially dehydroxylated at 200 °C under a high vacuum (10⁻⁵ mbar) for 2 h.

This supported catalyst was synthesized using surface organometallic chemistry (SOMC) grafting approach. The heterobimetallic precursor, PdZn(μ -OOCCH₃)₄, was obtained following the procedure reported by Kozitsyna et al [49].

The catalysts were produced starting from PdZn(μ -OOCCH₃)₄ (1.54 mmol) and the oxide (CeO₂, ZrO₂ or CeZrOx, 3 g, 5%wt Pd) in toluene for 4 h, stirred at 80 °C under an inert atmosphere. The titration of surface OH provided a concentration of 0.6 mmol/g for CeO₂, 0.21 mmol/g for CeZrOx and 0.15 mmol/g for ZrO₂. Then among the three studied supports, CeO₂ has sufficient surface OH groups to react with the amount of precursor (ca. 0.513 mmol Pd /g of oxide). However, the available surface OH groups of CeZrOx and ZrO₂ are in deficient with respect to the added precursor. Thus, part of the precursor is probably grafted and a quantity will be deposited for these two latter supports. Acetic acid was qualitatively observed by GC in the solution, testifying some grafting of the hetero bimetallic complex through protonolysis. However, due to the strong adsorbing nature of acetic acid on the basic supports, quantification was rather challenging. The solvent was evaporated and the sample was then calcined for 16 h at 500 °C under a flow of dry air, then cooled down under vacuum. Afterwards, the sample was reduced under a flow of H₂ at 400 °C for 3 h. Afterwards, the samples were stored in an inert atmosphere.

The same procedure was applied for the production of Pd@CeZrOx (5 %wt Pd) and Zn@CeZrOx (3 %wt Zn) using Pd(μ -OOCCH₃)₂ and Zn(μ -OOCCH₃)₂ as precursors.

SAPO-34(CAS: 1318-02-1) was purchased from ACS materials. The sample was calcined for 16 h at 500 °C under a flow of dry air.

2.2 Elemental analysis

Elemental analyses were performed by the Pascher Microanalysis Laboratory in Remagen, via ICP. Samples were sent there sealed under vacuum.

2.3 Surface area and porosity analysis

BET surface area analysis was run via N₂ adsorption at 77.185°K on a Micromeritics ASAP 2020 Surface Area and Porosity Analyzer, interfaced with the ASAP 2020 V3.04 program. This analysis allowed to quantify BET and Langmuir surface area, as well as pore volume and size.

2.4 Powder X-Ray Diffraction

Powder X-Ray Diffraction (PXRD) patterns were collected on a Bruker D8 Advance diffractometer with Bragg-Brentano geometry goniometer in Theta-Theta mode and Cu K α _{1,2} X-Ray source. Diffractograms were collected in 10-70° 2 θ range by ethanol dispersion over Silicon support and treated using DIFFRAC.EVA Bruker software.

2.5 Infrared spectroscopy

Fourier Transform Infrared Spectroscopy (FTIR) in Attenuated Total Reflectance (ATR) mode was used to characterize the evolution of the samples during the synthesis procedure by measuring spectra under inert atmosphere, i.e. by using a Bruker-Alpha spectrophotometer with diamond crystal directly inside the glove-box. Spectra were collected in a 4000-600 cm⁻¹ range with 2 cm⁻¹ resolution using a Deuterated TriGlycine Sulfate (DTGS) detector.

FTIR spectroscopy in transmission mode was instead employed to characterize surface properties of the catalysts by following the adsorption of CO used as probe molecule. Absorption/transmission FTIR spectra were collected using a Bruker Vertex 70 spectrophotometer equipped with a Mercury Cadmium Telluride (MCT) cryo-detector in the 4000-600 cm⁻¹ range with 2 cm⁻¹ resolution. Powders were pressed in self-supporting discs (~10 mg/cm²) and placed in quartz IR cells suitable for thermal treatments in controlled atmosphere and for spectra recording at room temperature (RT) and liquid nitrogen temperature (nominal LNT). Before IR measurements, catalysts underwent an activation procedure meant to simulate the catalyst calcination and reduction processes. In both cases the followed protocol started with: i) outgassing and heating of the catalyst from RT to 400°C at 5°C/min, ii) holding at 400°C for 30', iii) treating under O₂ (40 mbar) for 30' and iv) cooling down to RT under O₂. Reduction treatment was simulated prior treating the oxidised catalyst with H₂ (40 mbar) at 400 °C for 30' followed by cooling under vacuum. As presented the best conversion/selectivity results, FTIR spectra were collected only for PdZn alloy supported on CeZrOx. After the activation procedure, spectra of CO absorption at increasing pressure up to 40 mbar were collected at RT and 77K. Spectra were treated using Bruker OPUS spectroscopy software.

2.6 X-ray Photoelectron Spectroscopy (XPS)

Chemical characterization by XPS was carried out using a Versaprobe II spectrometer from ULVAC-PHI. A monochromatic microfocused beam (X-ray source Al-K α 1486.6 eV) of 100 μ m of diameter and 250W power was focused on the surface of the samples. The high-resolution and survey spectral analyses were performed using pass energy of 23.9 and 117 eV corresponding to a resolution of 0.6 and 1.6 eV, respectively. All XPS measurements were carried out in an ultra-high vacuum chamber (7.10⁻¹⁰ mbar). Each core level peak was recorded within a scan rate of 0.1 eV/s. The binding energy calibration was performed using Au4f_{7/2} (83.94 eV), Ag3d_{5/2} (368.2 eV) and Cu2p_{3/2} (932.6 eV). CasaXPS software was used for Ce 3d, Zn LMM and Pd 3d curve fitting. All were performed using pseudo-Voight function and corrected Shirley background for the former and linear background for the Zn and Pd regions.

2.7 X-Ray Absorption Spectroscopy (XAS)

EXAFS spectra were acquired at ESRF, Grenoble, France, using BM23 beam-line at the zinc K-edge in the transmission mode. For each sample, four scans were recorded, between 9.5 and 10.7 keV, at room temperature (295 K). Each data set was collected simultaneously with a Zn metal foil reference (9658.6 eV), [50] and was later aligned according to that reference (first maximum of the derivative of the Zn foil spectrum set at 9658.6 eV). The samples were packed in an argon-filled glovebox within an air-tight sample holder. The data analyses were carried out using the program "Athena" [51] and the

EXAFS fitting program “RoundMidnight”, from the “MAX” package [52], using spherical waves. The program FEFF8 was used to calculate theoretical files for phases and amplitudes based on model clusters of atoms [53]. The refinements were carried out by fitting the structural parameters N_i , R_i , σ_i and the energy shift, ΔE_0 (generally the same for all shells of a same phase). The S_0^2 parameter was set at the value proposed by FEFF8 program (0.92). For each fit, the quality factor, $(\Delta v)^2/v$, where v is the number of degrees of freedom in the signal, was calculated and its minimization considered in order to control the number of variable parameters in the fits [54].

2.8 Electron microscopy: TEM, STEM and EDX

Scanning Transmission Electron Microscopy - High Angle Annular Dark Field (STEM-HAADF) images were obtained in a probe-corrected Titan Low Base (FEI) at a working voltage of 300 kV, coupled with a HAADF detector (Fischione) available at the “Advanced Microscopy Laboratory (LMA)” of the University of Zaragoza. X-ray Energy Dispersive Spectra (EDS) were obtained with an EDAX detector. The samples were dispersed in toluene and a small amount of solution was deposited on a Cu-carbon grid.

2.9 Catalytic tests

CO₂ conversion was performed in Microreactivity (PID, Micrometric) reactor equipped with a furnace (max. temperature = 700 °C), Bronkhorst massflow controllers and a back-pressure regulator. The ½” stainless steel reactor was placed in the furnace inside a hot box (max. temperature = 150 °C) allowing pre-heating of the gas and avoiding condensation in the outlet lines. The catalytic bed is comprised of the catalyst in powder form (grain size of the catalyst powder: 15-20 nm, grain size of the SAPO-34: 3-5 µm). The reactor contains a 4-way valve, the catalyst can then be charged in the glovebox and the gas lines can be extensively purged with the reactant gas before exposing to the catalyst. A certified gas cylinder (Mélange Crystal, Air Liquide) with H₂/CO₂ ratio of 3 was used. The reactor was first pressurized to the desired pressure (up to 30 bar) before the heating was started (10 °C/min). The post-reactor lines were heated to 150 °C to minimize condensation of the product and connected to an online GC (Agilent 7890A) equipped with two columns in series (PLOT Q and Carbon Plot, the latter in store column configuration). The products were detected by TCD and FID (equipped with Jetanizer™) connected in series. The conversion and selectivity values were obtained using the following formulas:

$$Conversion = \frac{\text{Total mol of products}}{\text{Total mol in effluent}} * 100$$

$$Selectivity\ in\ Cn = \frac{n * \text{Total mol of } Cn}{\sum (n * \text{Total mol of } Cn)} * 100$$

The carbon balance is close to 100% when taking into account instrumental errors (typically around 5% for GC).

3. Results and Discussion

3.1 Supported PdZn nanoparticles through surface organometallic chemistry

3.1.1 From the complex to the supported PdZn nanoparticles.

Successful deposition and reduction of [PdZn(μ-OOCMe)₄]₂ was monitored by ATR spectroscopy using the acetate complex spectra reported in **Figure S1** as reference spectra. Whilst after grafting acetates

vibration modes, discussed in detail in Table S1, are observed over catalysts surface, they are consumed after reduction process (**Figure S2**). This result, combined with the multiple Pd and Zn signals in the XPS scans (vide infra) and the PdZn Bragg Reflection in the diffractogram (**Figure 2**), confirms bimetallic alloy formation parallel to the acetate complex thermolysis. ATR-FTIR is based on the interaction between the evanescent wave and the sample. The former consists only of a little part of the incoming beam and penetrates few μm in the sample. Since the particle size is observed to be in the nm scale (Figure S8) in this case ATR can be considered as a bulk technique reducing the surface-to-bulk signal. As clearly visible in **Figure S2**, ATR-FTIR spectra shows only features of very intense band (i.e., abundant acetates) whilst it does not provide sufficient information on the OH stretching region. To deeply investigate molecule-to-support interactions we then characterized PdZn@CeZrOx, the most promising catalyst (vide infra) by FTIR spectroscopy in transmission mode.

Absorption/transmission FTIR spectra of the PdZn@ CeZrOx synthesis steps unveiled a variation in the OH stretching region parallel to acetate band formation appeared between $1650\text{-}1300\text{ cm}^{-1}$ (**Figure 1**. a) Absorption/transmission FTIR spectra of CeZrOx support after: i) hydroxyl groups normalization (grey), ii) $[\text{PdZn}(\mu\text{-OOCMe})_4]_2$ grafting and deposition (yellow), iii) calcination under O_2 (purple) and iv) reduction under H_2 (blue). Spectra of reference CeZrOx reduced is reported in red for clarity. b) Detail of OH stretching region. **Figure 1a** and **1b** pinpointing as grafting occurs to the detriment of terminal and bi-bridged OH groups at 3687 and 3650 cm^{-1} , respectively [55]. Calcination process restored partly OH vibrations collateral to acetate consumption (purple spectra, **Figure 1**), whilst reduction induced formation of $\text{Ce}^{+3} \text{ } ^2\text{F}_{5/2} \rightarrow ^2\text{F}_{7/2}$ electronic transition at 2127 cm^{-1} (blue spectra, **Figure 1a**) indirectly unveiling presence of oxide-related bulk oxygen vacancies (V_O) [56]. In order to obtain deeper information on the catalytic sites available on the catalyst surface before and after PdZn alloy formation, i.e. metallic and Lewis sites, we then probed the surface by CO adsorption.

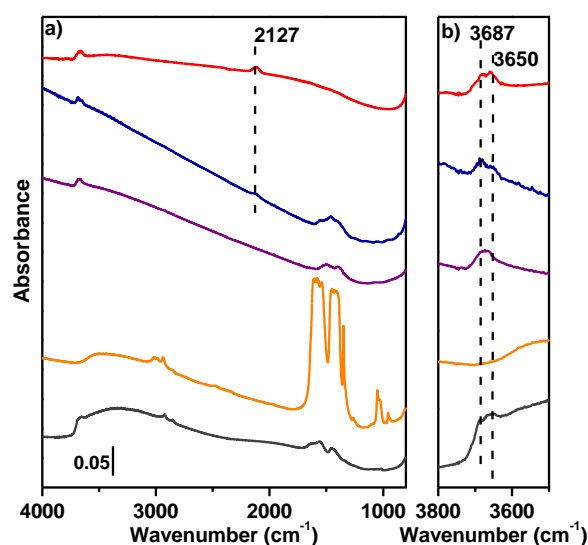


Figure 1. a) Absorption/transmission FTIR spectra of CeZrOx support after: i) hydroxyl groups normalization (grey), ii) $[\text{PdZn}(\mu\text{-OOCMe})_4]_2$ grafting and deposition (yellow), iii) calcination under O_2 (purple) and iv) reduction under H_2 (blue). Spectra of reference CeZrOx reduced is reported in red for clarity. b) Detail of OH stretching region.

As supporting samples, $[\text{PdZn}(\mu\text{-OOCMe})_4]_2$ grafting and calcination over pure CeO_2 and ZrO_2 were followed by ATR spectroscopy, showing the same behavior as PdZn@CeZrOx (**Figure S2**).

3.1.2 Composition, structure, and texture of PdZn nanoparticles: basic characterization

CeO_2 , ZrO_2 and CeZrOx presented good crystallinity after grafting and calcination, as evidenced by the PXRD patterns in **Figure S3**. Due to crystallite dimension-induced peak broadening, we cannot safely distinguish between cubic and tetragonal polymorphs. Thus, the most common structures for the three supports were used for simulation: cubic (Fm-3m) for CeO_2 [57], tetragonal ($\text{P4}_2/\text{nmc}$) for CeZrOx [58] and tetragonal/monoclinic ($\text{P4}_2/\text{nmc}$ and $\text{P2}_1/\text{c}$) mixture for ZrO_2 [59,60]. For the latter tetragonal-to-monoclinic ratio was evaluated as 50:50 using the equation proposed by Evans et al. [61] reported for clarity in SI together with the peak fit in **Figure S4**.

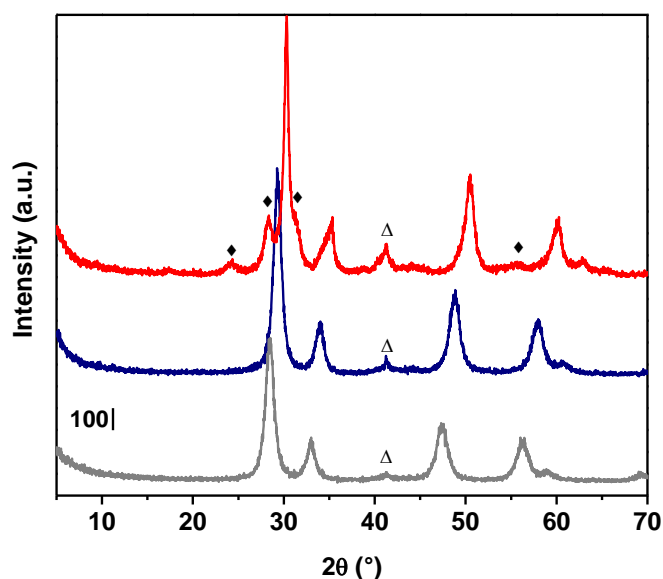


Figure 2. PXRD patterns of $[\text{PdZn}(\mu\text{-OOCMe})_4]_2$ grafted/deposited and reduced under H_2 on c- CeO_2 (gray), t- CeZrO_x (blue) and m/t- ZrO_2 (red), diamonds indicate monoclinic reflections. Triangles indicate PdZn alloy Bragg reflection.

The characterization of the reduced bimetallic catalyst, PdZn/CeZrO_x by X-ray diffraction revealed the presence of a Bragg reflection at ca. 41° in the diffractogram (**Figure 2**) [62,63], confirming the formation of a supported bimetallic Pd_{1-x}Zn_x alloy after thermolysis under hydrogen [46]. Similar features were observed for PdZn supported on CeO₂ and ZrO₂ (**Figure S3**). However, among the various existing PdZn alloy phases [64], several of them show a Bragg reflection in this 2θ range [65]. Due to low PXRD pattern resolution it is then not possible to specify the alloy phase, i.e. tetragonal β1 phase (P4/mmm space group; Pd_{1-x}Zn_x with x = 0.36 to 0.51), or palladium rich cubic β'' phase or a mixture of different alloy phases [66]. The β1 phase should present two Bragg diffraction peaks in the 40-45° 2θ range for (101) type planes and (110) type planes in a 10/4 ratio at ca. 41.3 and 44.1° and a cubic structure only one. A less intense peak at ca. 44° may exist but is difficult to observe on the diffractograms (**Figure 2**). The material was further characterized by XAS in order to try to specify the type of PdZn alloy present in the material (see below). Noteworthy, Bragg reflections from segregated ZnO, previously observed by preparing PdZn/ZrO₂ through colloidal impregnation synthesis [47], have not been observed, suggesting as SOMC techniques increased PdO/ZnO surface dispersion hence improving PdZn alloy formation.

The textural properties of the bare support and reduced sample are compared in **Table 1**. The adsorption/desorption isotherms are reported in the supplementary information (**Figure S7**) and show hysteresis loop characteristic of mesoporous materials. It is important to underline that the specific

surface area and the pore volume of PdZn/CeZrOx somewhat decrease after immobilization of the bimetallic alloy (see Table S2). Similar features were observed for PdZn supported on CeO₂ and ZrO₂ (Table S1 and Figure S5-S6).

Table 1 Superficial area, pore volume and pore diameter obtained for the treated support CeZrOx and for the reduced catalyst

	CeZrOx	PdZn@CeZrOx
BET SA (m²/g)	101.4	83.2
BJH pore volume (cm³/g)	0.24	0.18
BJH pores diameter (nm)	6.87	6.47

TEM was used to characterize PdZn/CeZrOx. This technique normally allows to acquire information about the particle size distribution of the samples. In this case, as shown in picture **Figure S7**, no sign of metallic particles or alloy was clearly observed due to the heavy support (notably the presence of Ce as well as Zr) which will absorb most of the electron beam and mask the lighter elements (Pd and Zn). No intuitive improvement was observed in the dark field mode (STEM HAADF). Nevertheless, the coupling of the microscopy with EDX analysis still provides insight about the elemental composition of the catalyst, though this method remains local and extremely selective dependent on the analyzed spot. The sampling of different points can in fact be used to verify the homogeneity in the composition of the bimetallic nanoparticles and its homogeneous distribution on the surface. Interestingly, all of the sampled points show correspondence between Pd and Zn. The technique also allows a quantification of these metals. EDX analyses on multiple zones revealed that the Zn/Pd ratio lies around 1, with an average value of 1.2 having a relatively high standard deviation (0.6). The inhomogeneity is most likely due to the presence of different metallic phases. The presence of PdZn alloy was confirmed by XRD. However, it was reported that monometallic Pd core can exist due to incomplete alloying [62]. Elemental analysis (ICP) is a far more reliable method to determine the bulk composition than TEM/EDX. ICP analysis of the sample proved that the bulk composition of the material (Pd = 5.07 wt%; Zn 3.10 wt%) maintain the desired 1:1 ratio between Zn/Pd (Table S3). The bulk composition of Zn/Pd is found to be 1. Nevertheless, the heterogeneity seems to be more pronounced for PdZn supported on CeO₂ and ZrO₂, suggested by TEM-EDX (Table S4).

3.1.3 Advanced characterization: XPS, CO adsorption followed by IR and X-Ray absorption spectroscopy

3.1.3.1 X-Ray Photoelectron Spectroscopy

A careful investigation of Ce and Pd 3d regions and Zn LMM Auger lines, reported in **Figure 3**, gave a valuable information on the element's oxidation states and their chemical surroundings. Ce3d(5/2) region of PdZn@CeZrO_x (**Figure 3a**) presented an high surficial concentration of Ce³⁺. Even if presence of Ce³⁺ in CeZrO_x support was already observed by IR spectroscopy (**Figure 1**), this technique probed both catalyst surface and bulk. On the contrary XPS signal is limited to the catalyst surface, unveiling that CeZrO_x support possess a higher surface Ce³⁺(V_o) concentration than pure CeO₂. This is qualitative observable from the relative intensities difference between Ce³⁺ (v₀ and v') and Ce⁴⁺ (v and v'') electronic transitions (**Figure 3a, S10**) [67]. CeZrO_x solid solutions are well known to present a considerable concentration of Ce⁺³ i.e., oxygen vacancies, due to the ionic radii difference between Zr and Ce atoms [68].

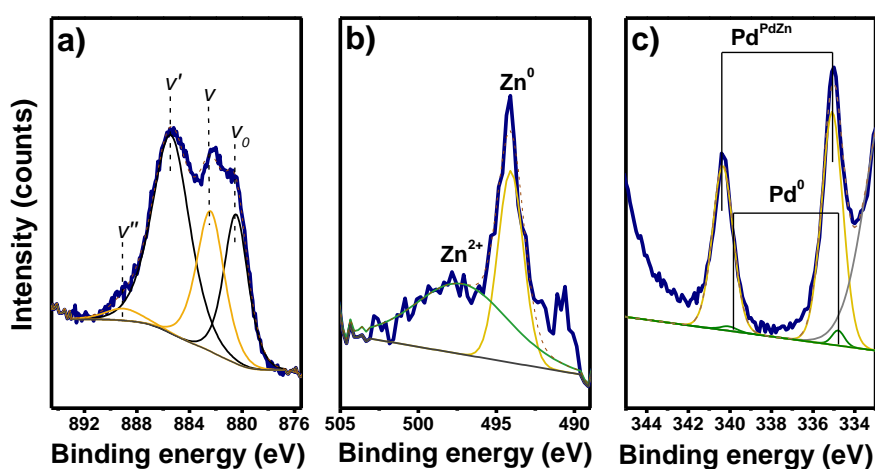


Figure 3. High resolution XP spectra of PdZn/CeZrO_x: a) Ce 3d(5/2), b) Zn 2p and c) Pd 3d regions. Experimental and best fit curves are represented by blue and dashed brown lines, respectively. Ce+3 (yellow line), Ce+4 (black line), metallic Zn/Pd alloy (yellow), ionic Zn (dark green) and Pd metal (green) components are reported.

While Zr oxidation state (+4) was clearly identified from its 3d region (Figure S11 b), metallic Zn and ionic ZnO cannot be distinguished from the Zn 2p spectra (Figure S11 a) due to their low energy shift (≈ 0.3 eV) [69]. For this purpose, Zn LMM auger line reported in **Figure 3 b** and S12 is more informative. Two components were observed at among 494 and 497 eV (Binding Energy) which can be associated to two chemical environments for Zn atoms. The associated Wagner parameters $\alpha' = E_k(\text{LMM}) + E_b(2p_{3/2})$, where E_k and E_b are kinetic and binding energies, respectively, are 2013 eV and 2010 eV, signatures of metallic and ionic Zn, respectively [70]. Presence of the alloy induces an inter atomic electron transfer and a Pd orbitals rehybridation, which shows as direct consequence a shift of Zn(2p) and Pd(3d) levels to lower and higher binding energies, respectively [71–77]. Moreover, Pd and Zn alloying induced electronic perturbation which is also clearly observed from CO adsorption discussed

in the following section. The energy shift, respect to the usual metallic/oxidic position, observed for the Zn 2p bands (Figure S11a) [69], is very clear in the Pd one 3d region. Pd 3d region (**Figure 3 c**) seems to present a single intense doublet, i.e., Pd 3d 5/2 and 3/2. However, a careful consideration of the energy positions and a direct comparison with reference PdZn@ZrO₂/CeO₂ (Figure S13 and Table S5) unveiled as a weak contribution from metallic Pd 3d(5/2) component can be identified at fixed BE of 334.8 eV while the intense band at 335.1 eV is associated to alloyed Pd, reported as Pd^{δ-} due to the charge transfer aforementioned. Noteworthy, a higher concentration of Ce⁺³, Zn(0) and Pd^{PdZn} was observed in PdZn@CeZrOx respect to PdZn@ZrO₂/CeO₂ (Figure S10, S12, S13), unveiling a higher concentration of oxygen vacancies and PdZn alloy.

3.1.3.2 CO adsorption followed by IR

Carbon monoxide is employed since decades as simple accessible probe molecule to investigate the chemical nature of surface sites. Once CO interacts with metal/ions sites on the catalyst surface, depending on the cation ionic potential, the predominant charge withdrawing direction can be divided into CO-to-metal or metal-to-CO, defining the interaction as σ -donation or π -backdonation, respectively [78,79]. The former depletes charge density from CO slightly antibonding level, increasing its bond strength and causing a hypsochromic shift from the ideal CO stretching vibration (2143 cm⁻¹), whilst the latter fills CO strongly antibonding levels, weakening the triple bond and inducing a bathochromic shift. Typically, for cationic sites σ -donation prevails, for metallic sites π -backdonation prevails, thus causing blueshift and redshift, respectively, of the stretching vibration of adsorbed CO. As a consequence, CO adsorption allows to determine whether: a) strong and weak Lewis acid sites (Ce⁴⁺ and Zr⁴⁺), necessary for CO₂ adsorption as carbonates [80,81], are still present over the catalyst surface after grafting and reduction treatments (blueshifted bands) and b) if the metallic PdZn alloy was formed at the surficial scale (redshifted bands with peculiar features).

Room Temperature CO adsorption. At RT CO is mainly adsorbed on strongly interacting sites i.e., Pd^{0/2+}. As calcination was conducted under O₂ atmosphere, from RT CO adsorption (**Figure 4a**) we expected to observe presence of PdO. However, a sharp band pointed at 2090 cm⁻¹ and a broader one at 1926 cm⁻¹ were assigned to CO linearly and bridged coordinated, respectively, to Pd⁰, where π -backdonation prevails [82]. As a matter of fact, it is well reported in literature that Pd⁰ is frequently observed on oxidized samples when using CO as probe at RT as the latter can easily reduce Pd²⁺ [83]. Moreover, a weak band at 2048 cm⁻¹ is observed at low CO coverages which assignment is not trivial. It could be related to CO interacting either with Pd⁰ or with Pd⁰ sites in preformed PdZn alloy. In the former case, the band could be located at such low wavenumber as related either to Pd defect sites, such as corners, edges and kinks, and/or to Pd⁰ interacting with Ce³⁺, which causes an electron

transfer from Ce^{3+} to Pd^0 , reinforcing the back-donation from Pd to CO, i.e. increasing the redshift [83]. As PdZn alloy is formed under strong reducing conditions [62,63,84], the presence of PdZn nanodomains under oxidizing conditions is hard to proof and to believe. On the contrary, due to the CeZrOx solid solution [85], Ce^{3+} is present on the catalyst surface (vide infra).

PdO reduction by CO was confirmed by measuring the evolution of CO interaction with calcined PdZn@CeZrOx with rising the temperature from liquid nitrogen temperature (nominal LNT) to RT, reported in **Figure S14**. At nominal LNT, as also seen in the next session in **Figure 5** a large band at 2155 cm^{-1} indicates a convoluted contributions of CO interacting with $\text{Zr}^{4+}/\text{Ce}^{4+}$ and Pd^{2+} sites (**Figure S14a**). While temperature rises, CO desorbs from $\text{Ce}^{4+}/\text{Zr}^{4+}$ Lewis acid sites and selectively reduces PdO forming first Pd^+ and Pd^0 sites, unveiled by the presence of bands at 2131 and 2095 cm^{-1} related to CO linearly adsorbed over Pd^+ and Pd^0 , respectively [86]. Finally close to room temperature, only a band at 2095 cm^{-1} is observed, showing that all $\text{Pd}^{+/2+}$ sites have been reduced to Pd^0 . Moreover, a large band occurs at lower wavenumbers with main contributions at 1970 and 1920 cm^{-1} assigned to bridged carbonyls on Pd(100) and Pd(111) faces, respectively [82]. PdO reduction is accompanied by CO-to- CO_2 oxidation as shown by presence of symmetric and asymmetric stretching modes of monodentate (1504 and 1345 cm^{-1}), bidentate (1575 and 1299 cm^{-1}) carbonates and bicarbonates (1619 and 1393 cm^{-1} , $\delta(\text{OH})$ at 1219 cm^{-1}) in **Figure S14b**. [87]

CO adsorption at RT over reduced catalyst (**Figure 4b**) showed a single asymmetric band at 2062 cm^{-1} , red-shifted ($\Delta\nu \approx 30\text{ cm}^{-1}$) from the frequency of linear CO-Pd 0 observed for the calcined sample ($\approx 2090\text{ cm}^{-1}$). [83] This phenomena, well reported in literature [72–77,88], is a fingerprint of Pd in PdZn alloy since the Zn-to-Pd charge transfer, observed by XPS measurements, leads to a strengthening of the Pd(4d)-CO(2π) backdonation, shifting $\nu(\text{CO-Pd})$ from 2090 to 2062 cm^{-1} .

Band asymmetry is due to a component at lower wavenumbers that can be reasonably assigned to carbonyls of Pd 0 defect sites in the PdZn alloy nanoparticles and/or Pd 0 in the alloy and interacting with Ce^{3+} . As a matter of fact, along with Ce^{3+} sites due to the CeZrO $_x$ solid solution (vide infra) and those formed by the reduction at $400\text{ }^\circ\text{C}$, small amount of additional Ce^{3+} sites are reasonably formed by CO interaction. This is demonstrated by the small amount of carbonates formed during interaction with CO. Even if their amount is much lower than that observed for the calcined sample (Fig. S18), their formation is not negligible. The small amount of carbonates on the reduced sample can be ascribed to CO oxidation by the lattice oxygen of CeZrO $_x$ catalysed by supported PdZn alloy [89,90]

. This causes the formation of additional Ce^{3+} sites involved in an electron transfer to Pd 0 . It is worth noting the presence of a broad band in the region $1950\text{--}1750\text{ cm}^{-1}$ related to bridged CO-(Pd 0) $_2$ species. However, this species is not expected for Pd in the alloy, due to the lack of neighbouring Pd sites. The presence of this band indicates that nano-scaled Pd clusters, already observed by XPS (**Figure 3c**), are

present. Due to the lack of the corresponding band of linear carbonyls at 2090 cm^{-1} , it is reasonable that these Pd clusters occur on defect sites of the PdZn nanoparticles, such as the edges of the alloy, whose linear carbonyl absorption falls under the band at 2062 cm^{-1} . Noteworthy, CO is adsorbed selectively on Pd and not on Zn [91], therefore the blueshift of linear carbonyl band with respect to the calcined catalyst proved the alloy formation while the low amount of bridged carbonyls underlined the presence of low amount of Pd clusters and the prevalent Pd-Zn alternation on the catalyst surface.

In both spectra in **Figure 4**, a blueshift of the main band was observed at increasing CO partial pressure: from 2082 to 2090 cm^{-1} for the calcined catalyst (panel a) and from 2048 to 2062 cm^{-1} for the reduced catalyst (panel b). This shift is explained considering the so called “chemical effect”, i.e. when the surface coverage increases, CO σ -donation and π -backdonation contributions decrease, weakening the bond of CO with the site and shifting the CO vibration frequency at lower and higher frequencies, respectively, according to the dominating contribution [78,92]. In the case of Pd, the dominating contribution is the π -backdonation and a blueshift is observed.

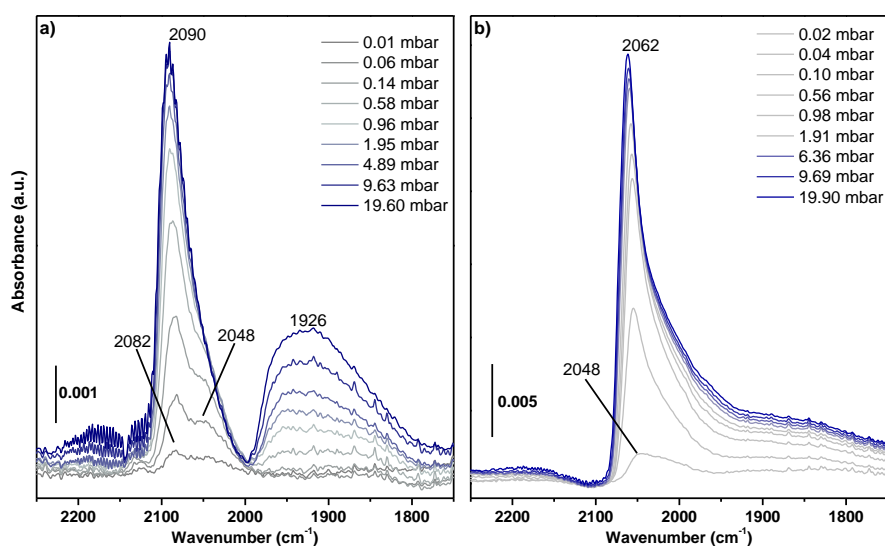


Figure 4. Absorption/transmission FTIR spectra of CO adsorbed at Room Temperature at increasing partial pressures over: a) calcined PdZn@CeZrOx and b) reduced PdZn@CeZrOx. Increasing CO partial pressure (grey to blue lines) are reported in both panels.

Liquid Nitrogen Temperature CO adsorption. Nominal LNT CO adsorption was carried out on calcined and reduced PdZn@CeZrOx, reported in **Figure 5a** and **b**, respectively, showed presence of very different Lewis and metallic sites on the two samples. Calcined catalyst (**Figure 5a**) presented a single sharp band at 2170 cm^{-1} which is redshifted to 2156 cm^{-1} by rising CO partial pressure. Band position, associated to CO interacting predominantly by σ -donation with $\text{Zr}^{4+}/\text{Ce}^{4+}$ and Pd^{2+} defect sites [93,94], is in agreement with presence of PdO nanodomains over CeZrOx surface. As in these sites, the σ -

donation is the prevalent contribution, at higher CO partial pressure, the redshift of the main band is explained considering the aforementioned “chemical effect” [78]. At low CO partial pressure is evident the presence of three extra bands (inset **Figure 5**) at 2128, 2088 and 2048 cm^{-1} . While the former is associated to CO interacting with Ce^{3+} , the latter two are assigned to Pd^0 more and less coordinated and not-or-in interaction with Ce^{3+} , respectively, as already observed in the RT spectra in Figure 4b. Presence of Ce^{3+} , above confirmed by XPS spectroscopy, is justified as doping CeO_2 lattice with Zr^{4+} induces strain, compensated with the formation of oxygen vacancies associated to Ce^{3+} formation [85]. On the contrary, observing Pd^0 indicates that in this particular sample, i.e. PdO nanodomains originated from $[\text{PdZn}(\mu\text{-OOCMe})_4]_2$ thermolysis, PdO is easily reduced during activation even under oxidising condition.

Two intense bands are observed from CO adsorption over reduced catalyst (**Figure 5b**). The one located at higher wavenumbers is again associated to $\text{Ce}^{4+}/\text{Zr}^{4+}$ sites whilst the second one, pointed at 2074 cm^{-1} , as discussed in the previous section, is associated to Pd^0 located in the intermetallic PdZn. As observed in the measurement at RT, the band asymmetry is associated to Pd^0 defect sites in the PdZn alloy and/or Pd^0 in the alloy and interacting with Ce^{3+} (2062-1950 cm^{-1}); the weak band in the region 1950-1800 cm^{-1} is related to bridged carbonyls formed on metallic Pd nanodomains. As σ -donation contribution prevails in CO- $\text{Ce}^{4+}/\text{Zr}^{4+}$, “chemical effect” causes a band redshift from 2162 to 2150 cm^{-1} when increasing CO partial pressure, while π -backdonation dominates for CO- Pd^0/PdZn interaction, leading to a blueshift of the band from 2062 to 2074 cm^{-1} . Presence of bulk Ce^{3+} was already observed from the electronic transition at 2127 cm^{-1} in **Figure 3**, while the band at 2128 cm^{-1} in **Figure 4b** unveiled the presence of Ce^{3+} also on the surface.

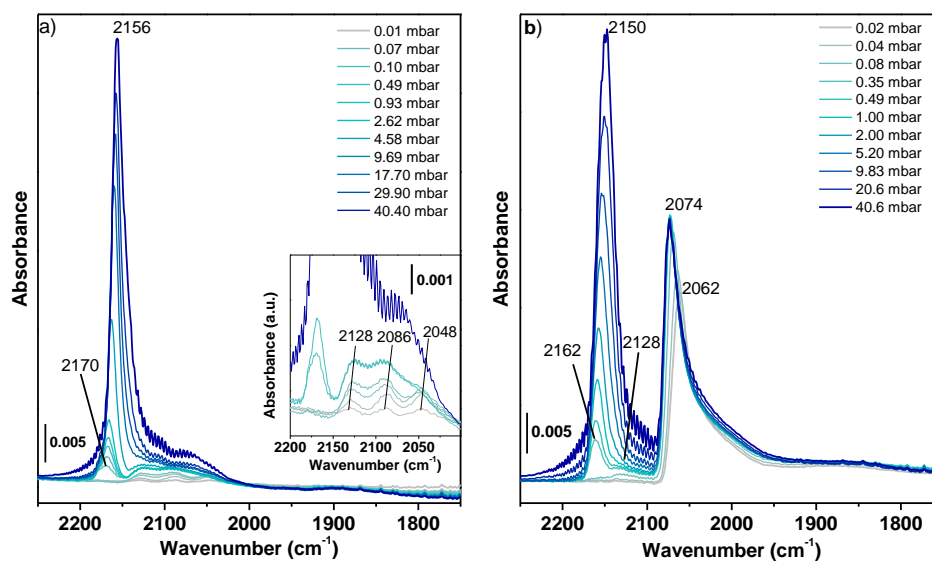


Figure 5. FTIR spectra of CO adsorbed at Liquid Nitrogen Temperature over PdZn@CeZrOx: a) calcined and b) reduced. Main Panels: Increasing CO partial pressure (grey to blue line) are reported in both panels. Bottom inset in a) detail of $\text{Ce}^{3+}/\text{Pd}^0$ region during stabilization at first pressure of 0.01 mbar.

3.1.3.3 X-Ray absorption spectroscopy

The PdZn/CeZrOx sample reduced under hydrogen was studied by X-ray absorption spectroscopy at the Zn-K edge in order to shed light on the structure of the supported species of zinc.

XANES analysis –

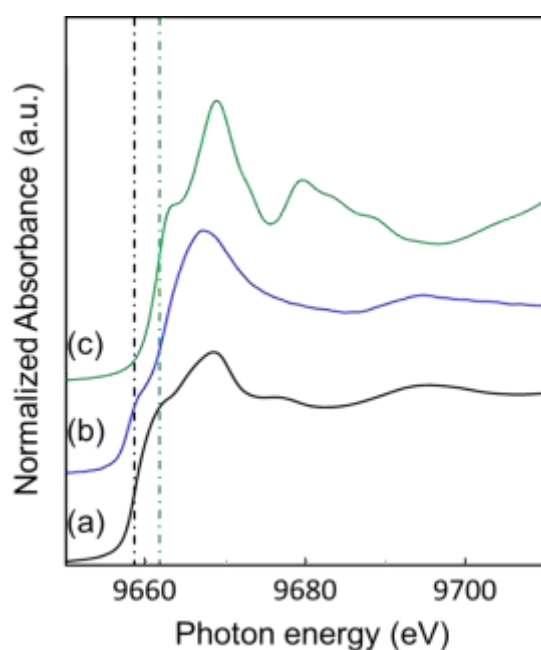


Figure 6. Zinc K-edge XANES for (a) zinc metal foil ($\text{Zn}(0)$); (b) reduced PdZn/CeZrOx; (c) ZnO ($\text{Zn}(\text{II})$).

From the XANES spectrum (**Figure 6**), it can be observed that the sample PdZn/CeZrO_x reduced present two inflexion points at 9658.0 and 9662.2 eV, energy values close to those observed respectively for Zn metal (Zn(0), positioned at 9658.6 eV, and for ZnO (Zn(II)), at 9661.6 eV, thus suggesting strongly that zinc exists in two different phases with two different oxidation states in this sample. This agrees with a bimodal distribution of zinc, between a PdZn alloy and possibly single-sites grafted on the CeZrO_x support or ZnO particles.

EXAFS analysis –

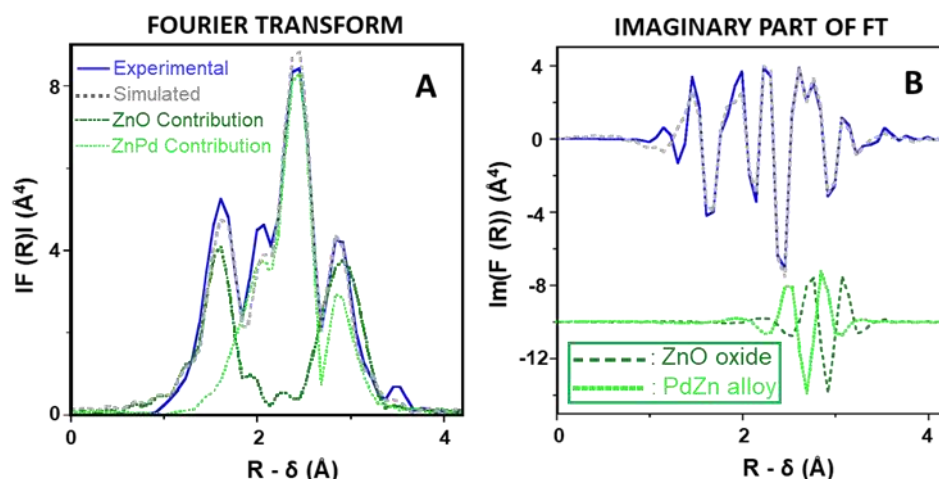


Figure 7. (A): Modulus of the Fourier transform of the k^3 -weighted Zn K-edge EXAFS of reduced PdZn/CeZrO_x, with the contributions of ZnO (dark green) and ZnPd alloy (light green) phases; (B): imaginary part of the Fourier transform with the Zn--Zn contributions of the ZnO and ZnPd alloy phases. Solid lines: From experimental data; dashed lines: curve fit obtained with spherical wave theory.

The fit of the EXAFS signal of PdZn/CeZrO_x reduced sample was carried out from the filter of the FT of the real extracted signal ($k^3 \cdot \chi(k)$) between 0.5 and 3.4 Å. The corresponding curves are shown in **Figure S15** and **Figure 7** and the parameters obtained from the fit are given in **Table 2**.

Table 2 $k^3 \cdot \chi(k)$ EXAFS curve fit parameters for PdZn@CeZrO_x after reduction.^(a)

Neighboring Atom of Zn	Number of Atoms N	Distance from Zn R(Å)	Debye-Waller Factor $\sigma^2(\text{Å}^2)$
Zn-O^(b)	1.0(2)	1.96(2)	0.0014(8)
Zn-Pd^(c)	5.3(4)	2.598(8)	0.0103(10)
Zn--Zn^(c)	2.7 ^(d)	2.99(3)	0.0090(19)
Zn--Zn^(b)	3.0 ^(d)	3.22(3)	0.0094(20)

^(a) The errors on the last digit, generated by the EXAFS fitting program “RoundMidnight” are indicated in parentheses; Δk : [1.9 -14.7 Å⁻¹] - ΔR : [0.6-3.3 Å]; S_0^2 = 0.92; Fit residue: ρ = 5.2%; Quality factor: $(\Delta\chi)^2/\nu$ = 3.25,

with $v = 12/24$. ^(b) From a ZnO phase, $\Delta E_{01} = 2.6 \pm 1.9$ eV (fitted); ^(c) From a PdZn alloy phase, $\Delta E_{02} = 2.2 \pm 1.2$ eV (fitted); ^(d) Shell constrained to a parameter above.

The first peak in the FT (below 2 Å in **Figure 7**) could be fitted by light back-scatterers, ca. one oxygen atom at 1.96(2) Å which is in good agreement with values observed for ZnO wurtzite-type crystals ($3 \times 1.9738 - 1 \times 1.9884$ Å), [95] or for Zn-O distances observed from crystallographic data of molecular complexes which can be taken as model for isolated sites, in particular alkoxy types [96–101], in the 1.89 - 1.99 Å range. The highest peak in the FT (**Figure 7**) could be fitted by palladium metal back-scatterers, ca. 5.3 Pd atoms at a distance of 2.598(8) Å, which is slightly higher than the sum of the metallic radii of both Zn and Pd atoms (ca. 2.53 Å). In large crystals of Pd_{1-x}Zn alloys, usually longer Zn-Pd distances are observed by XRD: 2.638 Å for the tetragonal PdZn β₁ phase [66], but an average Zn-Pd distance as short as 2.538 Å could be observed for a Pd₂Zn phase [102]. Besides, by EXAFS, short Pd-Zn distances as 2.56 Å⁵⁶ and 2.61 Å [65] were found for PdZn alloys prepared from Pd(NO₃)₂/ZnO or {Pd(NO₃)₂+Zn(NO₃)₂}/Al₂O₃ materials after reduction by H₂. The fit was improved by adding two further layers of zinc, one corresponding to a PdZn alloy with 2.99(3) Å for Zn-Zn and the other corresponding to a ZnO phase at 3.22(3) Å, with a model considering PdZn and ZnO particles. It should be noted that these two scattering paths are in complete antiphase (lower part in **Figure 7B**). Though the second distance is perfectly in line with a ZnO phase,⁸² the first distance is higher than the one found for a Pd-Zn β₁ phase (2.88 - 2.92 Å) but distances as long as 3.055 Å can be found for other Pd-Zn alloys as Pd_{2.03}Zn_{0.97} [64]. This could indicate that the 1:1 stoichiometry is probably not uniform, as in PdZn β₁ phase (P4/mmm space group; Pd_{1-x}Zn_x with $x = 0.36$ to 0.51) [64]. Similar parameters were obtained when fitting $k^2 \cdot \text{Chi}(k)$ extracted signal (**Figure S16** and **Table S6**). Since at least two different phases are present in the sample, the interpretation of the EXAFS is delicate. However, the results seem to agree with the presence of ca. 25 % of Zn in a ZnO phase, with each zinc atom σ-bonded by four oxygen atoms at 1.96(2) Å and twelve zinc atom at 3.22(3) Å, and ca. 75 % of the zinc present in bimetallic particles of a Pd_xZn alloy. This would thus confirm the observations made from the XANES spectrum of the sample with two oxidation states for Zn.

3.2 Catalytic tests

The catalytic bed comprises a mechanical mixture of different catalysts and SAPO-34 in a 1:1 ratio (in weight). The results of the tests are resumed in **Table 3**.

The reaction conditions of 380 °C, 30 bar and 2000 GHSV was adapted based on literature reports. [103] Hybrid catalysts exhibited fairly high conversion (**Figure 8a**) and is about 24 % in all PdZn supported systems (**Table 3**). A notable amount of CO is formed, originated from the RWGS reaction, which is

endothermic and thus favored at higher temperatures. Thus, the different supports have apparently no effect on the conversion under the given conditions.

Table 3 Summary of Conversion and product selectivity of the catalytic tests on the different systems mixed with SAPO-34. Reaction conditions: 380 °C 30 bar and 2000 ml/g/h. *: Space velocity is 1000 ml/g/h **: Space velocity is 6000 ml/g/h.

Catalysts	Conv. (%)	Global Selectivity (%)					
		CO	CH ₄	C2	C3	CH ₃ OH	C4
PdZn@CeO ₂ SAPO-34	23.9	75.7	0	7.8	12.5	0.2	3.9
PdZn@ZrO ₂ SAPO-34	23.8	68.5	0.2	9.4	15.3	0.2	6.3
PdZn@CeZrOx + SAPO-34	23.9	48.4	0.2	15.1	27	0.3	8.9
PdZn@CeZrOx	30.3	95.8	0	0	0	4.2	0
PdZn@CeZrOx + SAPO-34*	24.2	28.3	0.2	27.6	36.8	0	7.1
PdZn@CeZrOx + SAPO-34**	23.9	61	0	12.4	18.5	0.4	7.7
ZnOx@CeZrOx SAPO-34	40.5	89.6	0	4.4	5.1	0	0.9
Pd@CeZrOx SAPO-34	70	0.1	99.8	0	0	0.1	0

All the hydrocarbons found in the products are saturated. This is probably due to the hydrogenating activity of Pd, able to hydrogenate the olefins that are produced nearby in the zeolite framework. Importantly, the relative selectivity in C2+ among the hydrocarbons is over 99%. The systems are very stable in the reaction conditions and no substantial deactivation over 15 h of testing is observed (**Figure 8**).

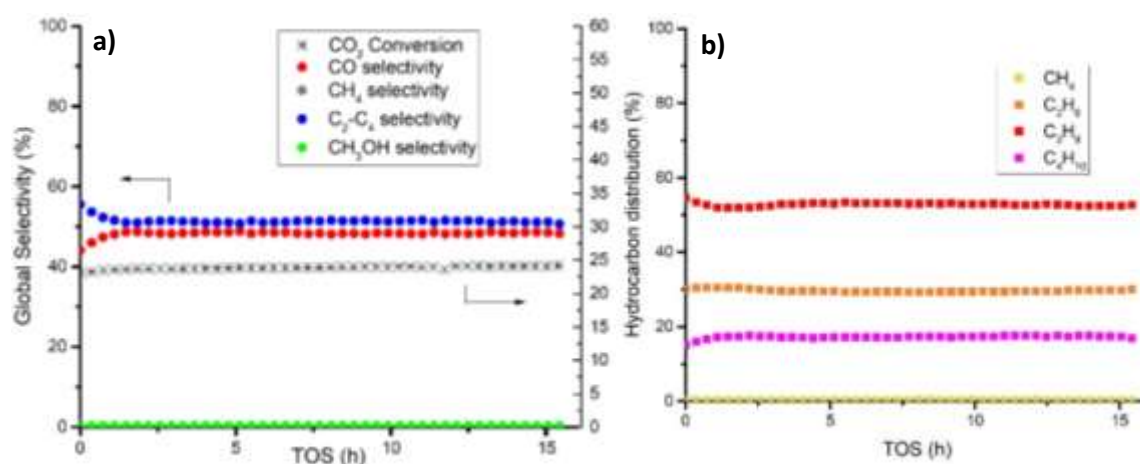


Figure 8. Conversion and product selectivity (a) and hydrocarbon distribution (b) vs. time on stream (TOS) during the catalytic tests on PdZn@CeZrO_x + SAPO-34. Reaction conditions: 380 °C, 30 bar and 2000 ml/g/h. A more detailed version of **Figure 9a** is present in the Supplementary Information (**Figure S17**).

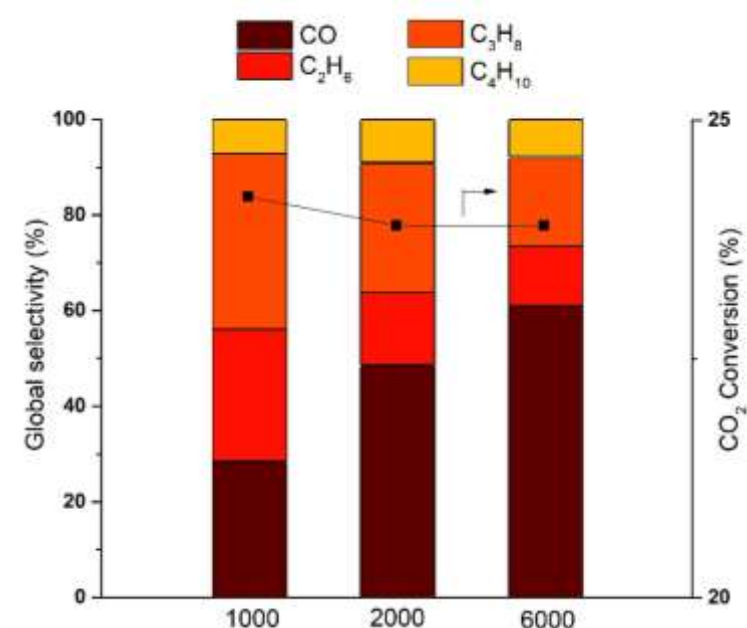


Figure 9. Conversion and products selectivities at different space velocities (ml/g/h) for the PdZn@CeZrO_x + SAPO-34. Reaction conditions: 380 °C, 30 bar (only traces of CH_3OH and CH_4 are formed, $S \leq 0.4\%$).

The PdZn@CeZrO_x + SAPO34 system is identified to be the most promising catalyst among the series exhibiting more than 50% global selectivity in hydrocarbons. Moreover, this system also showed the lowest amount of CO, as reported in **Table 3**: the selectivity in CO reaches ca. 76 % for PdZn/CeO₂, 68% for PdZn/ZrO₂ (see also **Figure S17**) and only ca. 48% for PdZn/CeZrO_x. Extensive studies were performed in order to further understand the role of each elements in the most promising system.

First of all, the bare support is inactive under the given conditions. Furthermore, Pd/CeZrOx (5 wt%) and ZnOx/CeZrOx (3 wt%) were prepared and submitted for catalytic investigation under the same conditions. ZnOx/CeZrOx leads to CO as main product, while Pd/CeZrOx gives selectively methane. These results suggest that the PdZn alloy is successfully formed for PdZn/CeZrOx by using the current synthesis approach. Nevertheless, the substantial amount of CO produced may indicate that a fraction of Zn migrated to the support during the catalyst preparation, as indicated by XPS, TEM/EDX and EXAFS. The tandem effect was also investigated by excluding the SAPO-34 from the bed. Under the same conditions, PdZn/CeZrOx gave unexpectedly high selectivity to CO (95%) and only 4% methanol. The extremely high selectivity to CO compared to the hybrid catalyst prompted us to elucidate the GHSV. Increasing the space velocity led to increase in the CO selectivity and evidently lower the hydrocarbon selectivity (**Figure 9**). Importantly, lower space velocity partly suppressed the CO production and increased the selectivity in the desired products. GHSV = 1000 presented the same conversion, but with a far lower selectivity in CO (28.3%) and high selectivity towards hydrocarbons (C₂+ = 71.5%). The reason is probably associated to the formation of water by the MTO reaction catalyzed by the zeolite that will trigger the water-gas shift reaction, resulting in the consumption of CO. The latter can be justified by comparing the conversion of the PdZn/CeZrOx with and without SAPO-34. Higher CO₂ conversion was observed in the absence of SAPO-34, suggesting that the water-gas shift reaction occur in the presence of SAPO-34. Matching conclusions were drawn from the testing of a similar system [47], which was produced in fairly different conditions (synthetic method, metallic ratios and loading), but presented analogous catalytic features. The PdZn/ZrO₂ + SAPO-34 reported in the article produced mainly saturated hydrocarbons and the effect on the WGS equilibrium was observed. The authors performed additional studies and attributed the presence of saturated hydrocarbons to the strong hydrogenating nature of PdZn alloy, while the kinetic studies led to the same conclusions on the WGS equilibrium that are reported in this paper.

4. Conclusions

PdZn/CeZrOx was carefully prepared and characterized through the loading of a heterobimetallic precursor, [PdZn(μ-OOCMe)₄]₂, partly by grafting on the mixed oxide OH groups and by a simple deposition of the excess of complex on the support. It was followed by a calcination and a reduction of this material. This unique preparation method provides an ideal starting point to form the necessary PdZn alloy, reported to be the desired phase for the selective hydrogenation of CO₂ to methanol, intermediate for the production of light hydrocarbons in the presence of SAPO-34. The reduced catalyst PdZn/CeZrOx was extensively characterized by various techniques. The supported PdZn phase was revealed by XRD. Supplementary XPS and EXAFS experiments indicated that there are two phases of Zn, assigned to a PdZn alloy phase as the major component accompanied by minor amount of

oxidized Zn, most probably ZnO. TEM-EDX analysis over several points showed that the Zn/Pd ratio was in average slightly below 1 with a fairly large standard deviation. The latter supports XPS and EXAFS data, suggesting that a minor, but notable amount of Zn escaped from the heterobimetallic precursor during the calcination and reduction, resulting in ZnO phase and PdZn alloy, with probably a core with monometallic Pd. Nevertheless, the bulk composition of Pd and Zn had the preferred ratio 1:1, as determined by elemental analysis. The presence of PdZn alloy is supported by in-situ FTIR at low temperature using CO as probe molecule. When combining PdZn/CeZrOx with SAPO-34, a tandem catalytic system for CO₂ conversion to hydrocarbons can be obtained. The latter system can readily transform CO₂ and H₂ to hydrocarbon with a conversion of 24% and high selectivity in light hydrocarbons (C₂-C₃: 82%). Virtually no deactivation of the catalyst was observed after 16 hours on stream. Controlled experiments were performed with Pd/CeZrOx and Zn/CeZrOx in order to gain supplementary insights of this system. Importantly, Pd/CeZrOx gave only methane and Zn/CeZrOx gave mainly CO under the same conditions. The latter clearly shows that the PdZn phase has an important impact for the production of hydrocarbons.

Acknowledgments

This project COZMOS has received funding from the European Union's Horizon 2020 research and innovation program under grant agreement No. 837733. In particular PR and DS are grateful for their PhD grant. MB is grateful to EU for an Erasmus grant and to CNRS for a complementary financial support during her Master internship at C2P2 Laboratory. LGJ (University of Tarragona, Spain) thanks BIZEOLCAT project (European Union's Horizon 2020 research and innovation program, grant agreement No. 814671) for a PhD grant. AdM (CNRS) thanks Olivier Mathon and Kiril Lomachenko for their help during the recording of the X-ray absorption spectra at ESRF, BM23.

References

- [1] T.R. Knutson, R.E. Tuleya, J. Clim. 17 (2004) 3477–3495.
- [2] J. Hansen, M. Sato, R. Ruedy, K. Lo, D.W. Lea, M. Medina-Elizade, Proc. Natl. Acad. Sci. 103 (2006) 14288–14293.
- [3] J. Yang, W. Cai, M. Ma, L. Li, C. Liu, X. Ma, L. Li, X. Chen, Sci. Total Environ. 711 (2020) 134569.
- [4] R. Ahmed, G. Liu, B. Yousaf, Q. Abbas, H. Ullah, M.U. Ali, J. Clean. Prod. 242 (2020) 118409.
- [5] L. Ansaloni, J. Salas-Gay, S. Ligi, M.G. Baschetti, J. Membr. Sci. 522 (2017) 216–225.
- [6] N. Mac Dowell, P.S. Fennell, N. Shah, G.C. Maitland, Nat. Clim. Change 7 (2017) 243–249.
- [7] Z. Wang, H. Song, H. Liu, J. Ye, Angew. Chem. Int. Ed. 59 (2020) 8016–8035.
- [8] R.M. Cuéllar-Franca, A. Azapagic, J. CO₂ Util. 9 (2015) 82–102.
- [9] Z. Jiang, T. Xiao, V.L. Kuznetsov, P.P. Edwards, Philos. Trans. R. Soc. Math. Phys. Eng. Sci. 368 (2010) 3343–3364.
- [10] Y. A. Daza, J. N. Kuhn, RSC Adv. 6 (2016) 49675–49691.

- [11] N. Ali, M. Bilal, M.S. Nazir, A. Khan, F. Ali, H.M.N. Iqbal, *Sci. Total Environ.* 712 (2020) 136482.
- [12] A. Galadima, O. Muraza, *Renew. Sustain. Energy Rev.* 115 (2019) 109333.
- [13] M.D. Garba, M. Usman, S. Khan, F. Shehzad, A. Galadima, M.F. Ehsan, A.S. Ghanem, M. Humayun, *J. Environ. Chem. Eng.* 9 (2021) 104756.
- [14] A.A. Olajire, *J. CO₂ Util.* 3–4 (2013) 74–92.
- [15] B. Grignard, S. Gennen, C. Jérôme, A. W. Kleij, C. Detrembleur, *Chem. Soc. Rev.* 48 (2019) 4466–4514.
- [16] J. Huang, R. Buonsanti, *Chem. Mater.* 31 (2019) 13–25.
- [17] L. Xu, Y. Xiu, F. Liu, Y. Liang, S. Wang, *Molecules* 25 (2020) 3653.
- [18] S. Das, J. Pérez-Ramírez, J. Gong, N. Dewangan, K. Hidajat, B. C. Gates, S. Kawi, *Chem. Soc. Rev.* 49 (2020) 2937–3004.
- [19] H. Yang, C. Zhang, P. Gao, H. Wang, X. Li, L. Zhong, W. Wei, Y. Sun, *Catal. Sci. Technol.* 7 (2017) 4580–4598.
- [20] G.A. Florides, P. Christodoulides, *Environ. Int.* 35 (2009) 390–401.
- [21] A. Ramirez, L. Gevers, A. Bavykina, S. Ould-Chikh, J. Gascon, *ACS Catal.* 8 (2018) 9174–9182.
- [22] S.G. Jadhav, P.D. Vaidya, B.M. Bhanage, J.B. Joshi, *Chem. Eng. Res. Des.* 92 (2014) 2557–2567.
- [23] I. Yarulina, A.D. Chowdhury, F. Meirer, B.M. Weckhuysen, J. Gascon, *Nat. Catal.* 1 (2018) 398–411.
- [24] I. Yarulina, K. De Wispelaere, S. Bailleul, J. Goetze, M. Radersma, E. Abou-Hamad, I. Vollmer, M. Goesten, B. Mezari, E.J.M. Hensen, J.S. Martínez-Espín, M. Morten, S. Mitchell, J. Perez-Ramirez, U. Olsbye, B.M. Weckhuysen, V. Van Speybroeck, F. Kapteijn, J. Gascon, *Nat. Chem.* 10 (2018) 804–812.
- [25] B. Zhao, P. Zhai, P. Wang, J. Li, T. Li, M. Peng, M. Zhao, G. Hu, Y. Yang, Y.-W. Li, Q. Zhang, W. Fan, D. Ma, *Chem* 3 (2017) 323–333.
- [26] M. D. Porosoff, B. Yan, J. G. Chen, *Energy Environ. Sci.* 9 (2016) 62–73.
- [27] W. Li, H. Wang, X. Jiang, J. Zhu, Z. Liu, X. Guo, C. Song, *RSC Adv.* 8 (2018) 7651–7669.
- [28] T.A. Atsbha, T. Yoon, P. Seongho, C.-J. Lee, *J. CO₂ Util.* 44 (2021) 101413.
- [29] P. Sharma, J. Sebastian, S. Ghosh, D. Creaser, L. Olsson, *Catal. Sci. Technol.* 11 (2021) 1665–1697.
- [30] P. Gao, S. Dang, S. Li, X. Bu, Z. Liu, M. Qiu, C. Yang, H. Wang, L. Zhong, Y. Han, Q. Liu, W. Wei, Y. Sun, *ACS Catal.* 8 (2018) 571–578.
- [31] Z. Li, J. Wang, Y. Qu, H. Liu, C. Tang, S. Miao, Z. Feng, H. An, C. Li, *ACS Catal.* 7 (2017) 8544–8548.
- [32] J. Wang, G. Li, Z. Li, C. Tang, Z. Feng, H. An, H. Liu, T. Liu, C. Li, *Sci. Adv.* 3 (2017) e1701290.
- [33] R. Raudaskoski, M.V. Niemelä, R.L. Keiski, *Top. Catal.* 45 (2007) 57–60.
- [34] X.-M. Liu, G.Q. Lu, Z.-F. Yan, *Appl. Catal. Gen.* 279 (2005) 241–245.
- [35] J. Słoczyński, R. Grabowski, A. Kozłowska, P. Olszewski, J. Stoch, J. Skrzypek, M. Lachowska, *Appl. Catal. Gen.* 278 (2004) 11–23.
- [36] J. Słoczyński, R. Grabowski, P. Olszewski, A. Kozłowska, J. Stoch, M. Lachowska, J. Skrzypek, *Appl. Catal. Gen.* 310 (2006) 127–137.
- [37] T. Phongamwong, U. Chantaprasertporn, T. Witoon, T. Numpilai, Y. Poo-arporn, W. Limphirat, W. Donphai, P. Dittanet, M. Chareonpanich, J. Limtrakul, *Chem. Eng. J.* 316 (2017) 692–703.
- [38] F. Liao, X.-P. Wu, J. Zheng, M.-J. Li, Z. Zeng, X. Hong, A. Kroner, Y. Yuan, X.-Q. Gong, S.C. Edman Tsang, *Catal. Sci. Technol.* 6 (2016) 7698–7702.

- [39] H. Bahruji, M. Bowker, W. Jones, J. Hayward, J. Ruiz Esquiús, D.J. Morgan, G.J. Hutchings, *Faraday Discuss.* 197 (2017) 309–324.
- [40] H. Bahruji, M. Bowker, G. Hutchings, N. Dimitratos, P. Wells, E. Gibson, W. Jones, C. Brookes, D. Morgan, G. Lalev, *J. Catal.* 343 (2016) 133–146.
- [41] J. Xu, X. Su, X. Liu, X. Pan, G. Pei, Y. Huang, X. Wang, T. Zhang, H. Geng, *Appl. Catal. Gen.* 514 (2016) 51–59.
- [42] F. Liao, X.-P. Wu, J. Zheng, M. Meng-Jung Li, A. Kroner, Z. Zeng, X. Hong, Y. Yuan, X.-Q. Gong, S.C. Edman Tsang, *Green Chem.* 19 (2017) 270–280.
- [43] A.S. Malik, S.F. Zaman, A.A. Al-Zahrani, M.A. Daous, H. Driss, L.A. Petrov, *Appl. Catal. Gen.* 560 (2018) 42–53.
- [44] O.A. Ojelade, S.F. Zaman, *Catal. Surv. Asia* 24 (2020) 11–37.
- [45] O.A. Ojelade, S.F. Zaman, M.A. Daous, A.A. Al-Zahrani, A.S. Malik, H. Driss, G. Shterk, J. Gascon, *Appl. Catal. Gen.* 584 (2019) 117185.
- [46] C. Ahoba-Sam, E. Borfecchia, A. Lazzarini, A. Bugaev, A. Adamu Isah, M. Taoufik, S. Bordiga, U. Olsbye, *Catal. Sci. Technol.* 10 (2020) 4373–4385.
- [47] A. Ramirez, P. Ticali, D. Salusso, T. Cordero-Lanzac, S. Ould-Chikh, C. Ahoba-Sam, A.L. Bugaev, E. Borfecchia, S. Morandi, M. Signorile, S. Bordiga, J. Gascon, U. Olsbye, *JACS Au* 1 (2021) 1719–1732.
- [48] I.S. Mashkovsky, *Mendeleev Commun.* 24 (2014) 355–357.
- [49] N.Y. Kozitsyna, S.E. Nefedov, F.M. Dolgushin, N.V. Cherkashina, M.N. Vargaftik, I.I. Moiseev, *Inorganica Chim. Acta* 359 (2006) 2072–2086.
- [50] J.A. BEARDEN, A.F. BURR, *Rev. Mod. Phys.* 39 (1967) 125–142.
- [51] B. Ravel, M. Newville, *J. Synchrotron Radiat.* 12 (2005) 537–541.
- [52] M. Alain, M. Jacques, M.-B. Diane, P. Karine, *J. Phys. Conf. Ser.* 190 (2009) 012034.
- [53] A.L. Ankudinov, B. Ravel, J.J. Rehr, S.D. Conradson, *Phys. Rev. B* 58 (1998) 7565–7576.
- [54] D.E. Sayers, the IXS Standards and Criteria Committee.
- [55] A. Laachir, V. Perrichon, A. Badri, J. Lamotte, E. Catherine, J. Claude Lavalley, J.E. Fallah, L. Hilaire, F.L. Normand, E. Quéméré, G. Noël Sauvion, O. Touret, *J. Chem. Soc. Faraday Trans.* 87 (1991) 1601–1609.
- [56] C. Binet, M. Daturi, J.-C. Lavalley, *Catal. Today* 50 (1999) 207–225.
- [57] C. Artini, M. Pani, M.M. Carnasciali, M.T. Buscaglia, J.R. Plaisier, G.A. Costa, *Inorg. Chem.* 54 (2015) 4126–4137.
- [58] T. Wakita, M. Yashima, *Acta Crystallogr. B* 63 (2007) 384–389.
- [59] P. Li, I.W. Chen, J.E. Penner-Hahn, *Phys. Rev. B* 48 (1993) 10063–10073.
- [60] Y. Kudoh, H. Takeda, H. Arashi, *Phys. Chem. Miner.* 13 (1986) 233–237.
- [61] J.G.P. Evans, P.A.; Stevens, R.; Binner, *Trans. J. Br. Ceram. Soc.* 83 (1971) 39–43.
- [62] M.W. Tew, H. Emerich, J.A. van Bokhoven, *J. Phys. Chem. C* 115 (2011) 8457–8465.
- [63] J. R. Gallagher, D. J. Childers, H. Zhao, R. E. Winans, R. J. Meyer, J. T. Miller, *Phys. Chem. Chem. Phys.* 17 (2015) 28144–28153.
- [64] H. Nowotny, E. Bauer, A. Stempf, *Monatshefte Für Chem. Verwandte Teile Anderer Wiss.* 82 (1951) 1086–1093.
- [65] ICSD web database FIZ Karlsruhe.
- [66] E.J. Peterson, B. Halevi, B. Kiefer, M.N. Spilde, A.K. Datye, J. Peterson, L. Daemen, A. Llobet, H. Nakotte, *J. Alloys Compd.* 509 (2011) 1463–1470.
- [67] E. Paparazzo, *J. Phys. Condens. Matter* 30 (2018) 343003.
- [68] B. Liu, C. Li, G. Zhang, X. Yao, S.S. Chuang, Z. Li, *ACS Catal.* 8 (2018) 10446–10456.
- [69] M.C. Biesinger, L.W.M. Lau, A.R. Gerson, R.S.C. Smart, *Appl. Surf. Sci.* 257 (2010) 887–898.

- [70] E. Lee, A. Benayad, T. Shin, H. Lee, D.-S. Ko, T.S. Kim, K.S. Son, M. Ryu, S. Jeon, G.-S. Park, *Sci. Rep.* 4 (2014) 4948.
- [71] J.A. Rodriguez, *J. Phys. Chem.* 98 (1994) 5758–5764.
- [72] C. Weilach, S.M. Kozlov, H.H. Holzapfel, K. Föttinger, K.M. Neyman, G. Rupprechter, *J. Phys. Chem. C* 116 (2012) 18768–18778.
- [73] C. Rameshan, W. Stadlmayr, C. Weilach, S. Penner, H. Lorenz, M. Hävecker, R. Blume, T. Rocha, D. Teschner, A. Knop-Gericke, R. Schlögl, N. Memmel, D. Zemlyanov, G. Rupprechter, B. Klötzer, *Angew. Chem. Int. Ed.* 49 (2010) 3224–3227.
- [74] K.M. Neyman, R. Sahnoun, C. Inntam, S. Hengrasmee, N. Rösch, *J. Phys. Chem. B* 108 (2004) 5424–5430.
- [75] H.P. Koch, I. Bako, R. Schennach, *Surf. Sci.* 604 (2010) 596–608.
- [76] A. Bayer, K. Flechtner, R. Denecke, H.-P. Steinrück, K.M. Neyman, N. Rösch, *Surf. Sci.* 600 (2006) 78–94.
- [77] K. M. Neyman, K. Hwa Lim, Z.-X. Chen, L. V. Moskaleva, A. Bayer, A. Reindl, D. Borgmann, R. Denecke, H.-P. Steinrück, N. Rösch, *Phys. Chem. Chem. Phys.* 9 (2007) 3470–3482.
- [78] A. Zecchina, D. Scarano, S. Bordiga, G. Ricchiardi, G. Spoto, F. Geobaldo, *Catal. Today* 27 (1996) 403–435.
- [79] K.I. Hadjiivanov, G.N. Vayssilov, *Adv. Catal.* 47 (2002) 307–511.
- [80] K. Pokrovski, K.T. Jung, A.T. Bell, (2001) 4297–4303.
- [81] C. Li, Y. Sakata, T. Arai, K. Domen, K. Maruya, 85 (1989) 929–943.
- [82] E. Groppo, S. Bertarione, F. Rotunno, G. Agostini, D. Scarano, R. Pellegrini, G. Leofanti, A. Zecchina, C. Lamberti, *J. Phys. Chem. C* 111 (2007) 7021–7028.
- [83] A. Bensalem, J.C. Muller, D. Tessier, F. Bozon-Verduraz, *J. Chem. Soc. - Faraday Trans.* 92 (1996) 3233–3237.
- [84] M. Gentzen, D.E. Doronkin, T.L. Sheppard, A. Zimina, H. Li, J. Jelic, F. Studt, J.-D. Grunwaldt, J. Sauer, S. Behrens, *Angew. Chem.* 131 (2019) 15802–15806.
- [85] B. Liu, C. Li, G. Zhang, X. Yao, S.S.C. Chuang, Z. Li, *ACS Catal.* 8 (2018) 10446–10456.
- [86] D. Tessier, A. Rakai, F. Bozon-Verduraz, *J. Chem. Soc. Faraday Trans.* 88 (1992) 741–749.
- [87] M. Daturi, C. Binet, J.C. Lavalley, G. Blanchard, *Surf. Interface Anal.* 30 (2000) 273–277.
- [88] K. Föttinger, *Catalysis* 25 (2013) 77–117.
- [89] A.A. Pawar, D. Lee, W.-J. Chung, H. Kim, *Chem. Eng. J.* 395 (2020) 124970.
- [90] G.S. Zafiris, R.J. Gorte, *J. Catal.* 139 (1993) 561–567.
- [91] J.A. Rodriguez, *Surf. Sci. Rep.* 24 (1996) 223–287.
- [92] P. Hollins, J. Pritchard, *Surf. Sci.* 89 (1979) 486–495.
- [93] C. Binet, M. Daturi, J.C. Lavalley, *Catal. Today* 50 (1999) 207–225.
- [94] C. Morterra, G. Cerrato, S. Di Ciero, *Appl. Surf. Sci.* 126 (1998) 107–128.
- [95] H.F. McMurdie, M.C. Morris, E.H. Evans, B. Paretzkin, W. Wong-Ng, L. Ettlinger, C.R. Hubbard, *Powder Diffr.* 1 (1986) 64–77.
- [96] K. Su, T.D. Tilley, M.J. Sailor, *J. Am. Chem. Soc.* 118 (1996) 3459–3468.
- [97] M. G. Gardiner, S. M. Lawrence, C. L. Raston, B. W. Skelton, A. H. White, *Chem. Commun.* 0 (1996) 2491–2492.
- [98] E. Bukhaltsev, I. Goldberg, A. Vigalok, *Organometallics* 23 (2004) 4540–4543.
- [99] E. Bukhaltsev, I. Goldberg, A. Vigalok, *Organometallics* 24 (2005) 5732–5736.
- [100] S. Jana, R.J.F. Berger, R. Fröhlich, T. Pape, N.W. Mitzel, *Inorg. Chem.* 46 (2007) 4293–4297.
- [101] R. Petrus, P. Sobota, *Acta Crystallogr. C* 68 (2012) m275–m280.

- [102] H.H. Stadelmaier, W.K. Hardy, *Int. J. Mater. Res.* 52 (1961) 391–396.
 [103] K. Bing Tan, G. Zhan, D. Sun, J. Huang, Q. Li, *J. Mater. Chem. A* 9 (2021) 5197–5231.

SUPPLEMENTARY INFORMATION

S1. Catalyst preparation

The heterobimetallic precursor $\text{PdZn}(\mu\text{-OOCCH}_3)_4$ has been prepared, inspired by a previous published method [1]. However, in order to improve the complex purity we worked under an inert atmosphere. To our knowledge, an IR spectrum of $[\text{PdZn}(\mu\text{-OOCMe})_4]_2$ has never been reported yet. Considering the respective literature for Pd and Zn acetates (Table. S1) [2,3], we here attempted a first band assignment of its ATR-FTIR spectrum which is reported in the 1800-400 cm^{-1} range and in the whole range in Fig. S1 and Table S1, respectively. All the bands were assigned to COO and CH_3 stretching and bending vibrations, respectively, related to a bridged acetate. As reported for Pd-acetate [3], the presence of terminal COO species is also observed by the weak $\nu(\text{C-O})$ and $\nu(\text{C=O})$ bands at 1260 and 1638 cm^{-1} , respectively. It should be noted that no bands attributed to water vibrations are presents in the ATR-FTIR spectrum, as expected since the precursor has been synthesized under anhydrous and inert conditions.

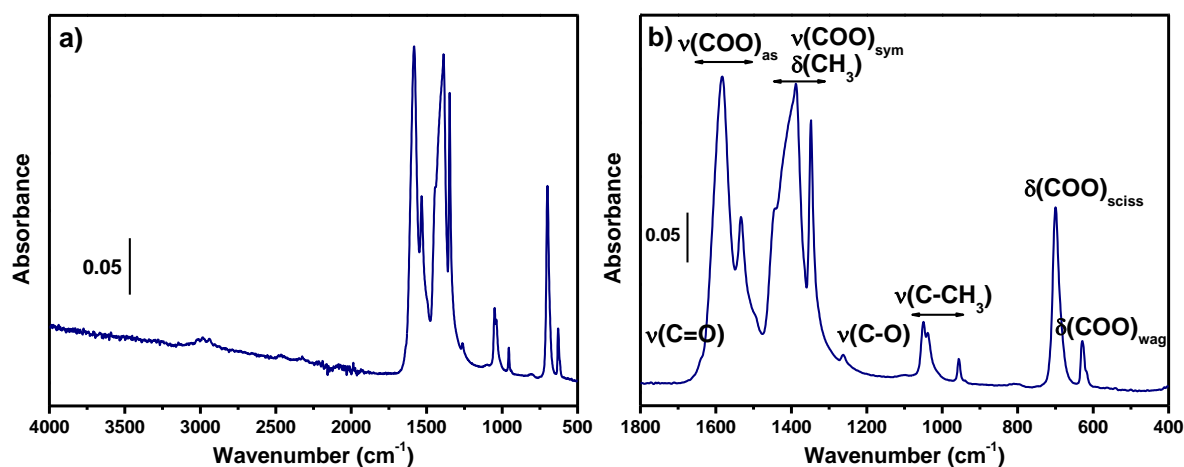


Figure S1. ATR-FTIR spectrum of $[\text{PdZn}(\mu\text{-OOCMe})_4]_2$ measured under inert atmosphere. a) full region of the spectra and b) detail of 1800-400 cm^{-1} region. Main stretching (ν) and bending (δ) vibration modes are indicated. “sciss” and “wag” indicate scissoring and wagging modes, respectively.

Table S1. IR active vibration modes for $\text{Pd}(\text{OOCMe})_2$ and $\text{Zn}(\text{OOCMe})_2$ reported from literature [4,5] and $[\text{PdZn}(\mu\text{-OOCMe})_4]_2$ observed in this work.^a

Vibrating group	$\text{Pd}(\text{OOCCH}_3)_2$ [5]	$[\text{PdZn}(\mu\text{-OOCCH}_3)_4]_2^a$	$\text{Zn}(\text{OOCCH}_3)_2$ [4]
$\delta(\text{COO})$ wagging	622	624	612
$\delta(\text{COO})$ scissoring	692	701	697
$\nu(\text{C-CH}_3)$	1020,1046	956, 1037, 1048	955, 1032, 1050
$\delta(\text{CH}_3)$	1332, 1372, 1392, 1430	1347, 1386, 1443	1343, 1415
$\nu(\text{COO})$ sym	1332, 1372, 1392, 1430	1347, 1386, 1443	1450
$\nu(\text{COO})$ asym	1604	1497, 1532, 1581	1565

S2. Characterization

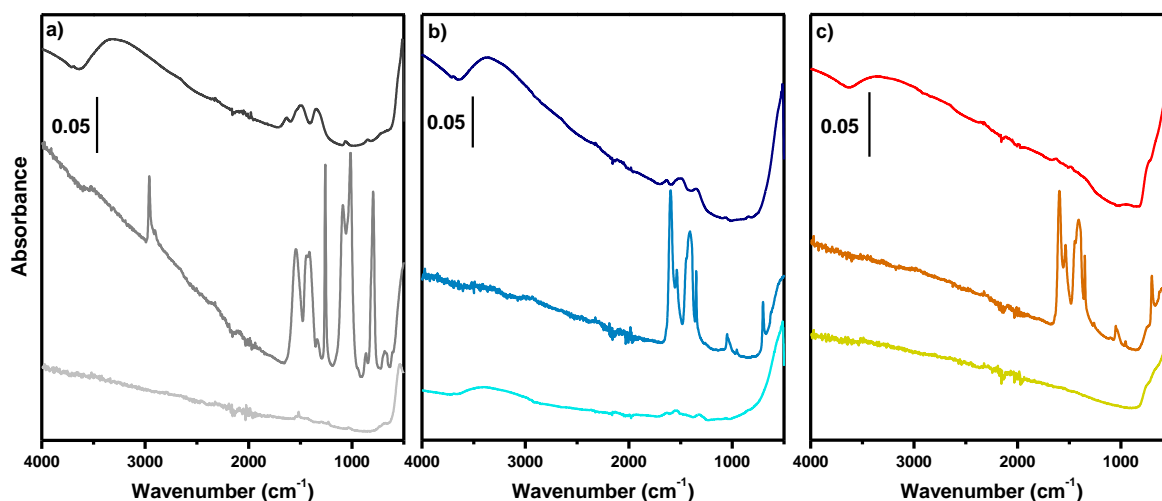


Figure S2. ATR-FTIR spectra of the a) c- CeO_2 , b) t- CeZrO_x and c) t/m- ZrO_2 supports as calcined, after $[\text{PdZn}(\mu\text{-OOCMe})_4]_2$ grafting and calcination (in order from the bottom) measured under inert atmosphere. Bands of residual toluene CH_3 ν_s and ν_{as} are observed at 2858 and 2934 cm^{-1} [6].

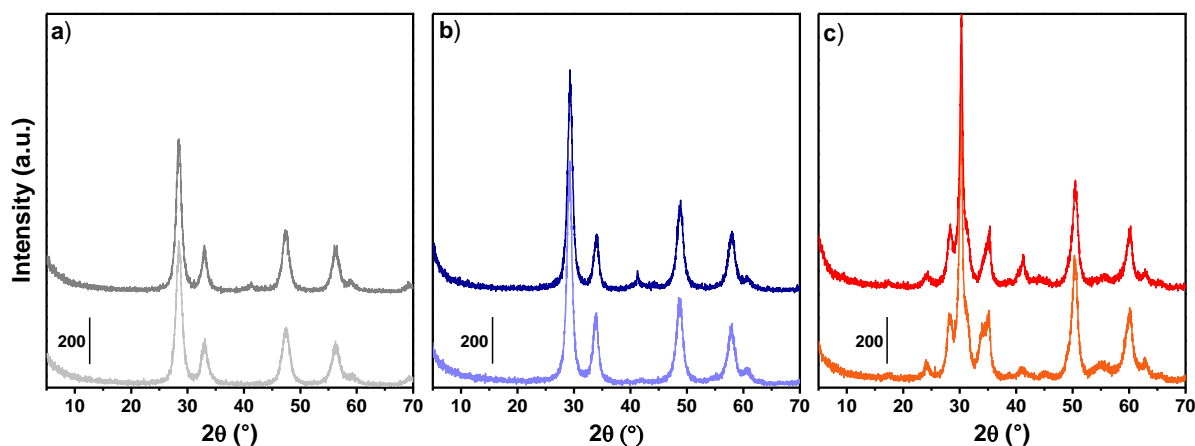


Figure S3. PXRD patterns of PdZn before and after H₂ reduction over a) c-CeO₂ (light gray and gray lines, respectively), b) t-CeZrO_x (light blue and blue lines, respectively) and c) t/m-ZrO₂ (orange and red lines, respectively).

$$\chi_M = \frac{I_M(111) + I_M(11\bar{1})}{I_M(111) + I_T(101) + I_M(11\bar{1})} * 100$$

Equation proposed by Evans et al.⁵ to quantify monoclinic (χ_M) and tetragonal ($\chi_T=100-\chi_M$) fractions considering the ratio between relative area of the monoclinic (111) and (11-1) reflections and the tetragonal (101) one, occurring at 28.3, 31.3 and 30.2°, respectively.

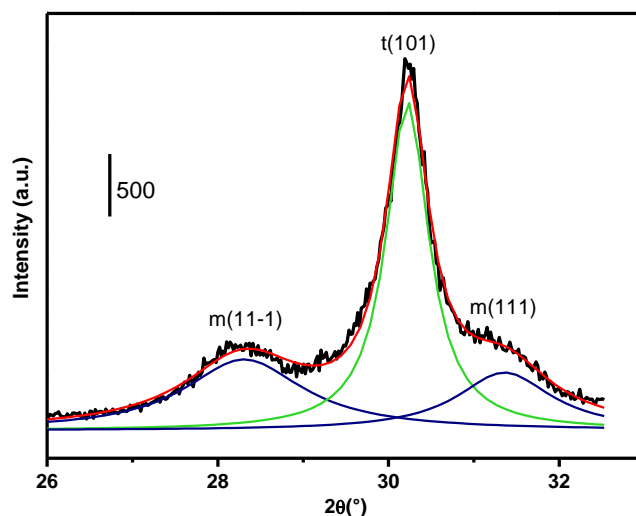


Figure S4. Detail of the m(11-1), m(111) and t(101) reflections regions. Lorentzian fit (red line) together with the monoclinic (blue lines) and tetragonal (green line) fits are shown.

Table S2. Superficial area, pore volume and pore diameter obtained for the treated supports: CeO₂, ZrO₂ and CeZrO_x.

	CeO ₂	PdZn@CeO ₂	ZrO ₂	PdZn@ZrO ₂	PdZn@CeZrO _x
		2		2	
BET SA (m²/g)	187.9	134.4	75.3	73.1	83.2

BJH pore volume (cm³/g)	0.23	0.15	0.12	0.08	0.18
BJH pores diameter (nm)	3.36	3.34	4.62	4.26	6.47

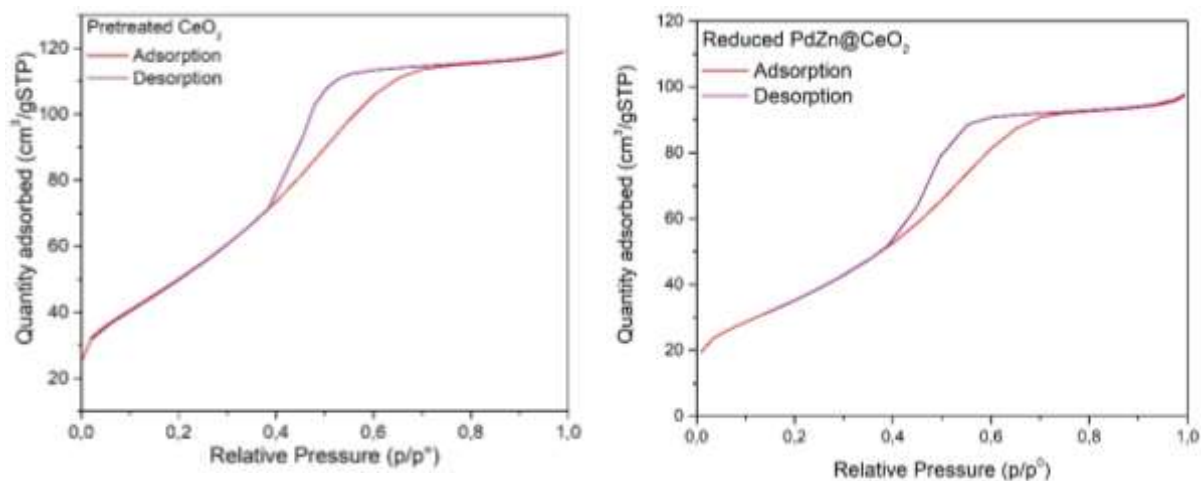


Figure S5. Isotherm linear plot of pretreated CeO₂ (left) and reduced PdZn@CeO₂ (right).

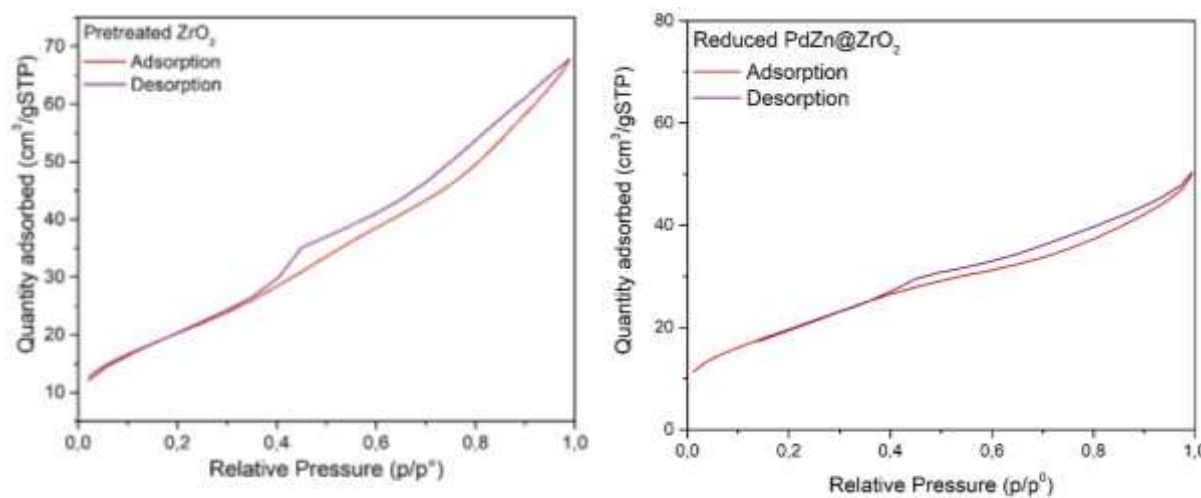


Figure S6. Isotherm linear plot of pretreated ZrO₂ (left) and reduced PdZn@ZrO₂ (right).

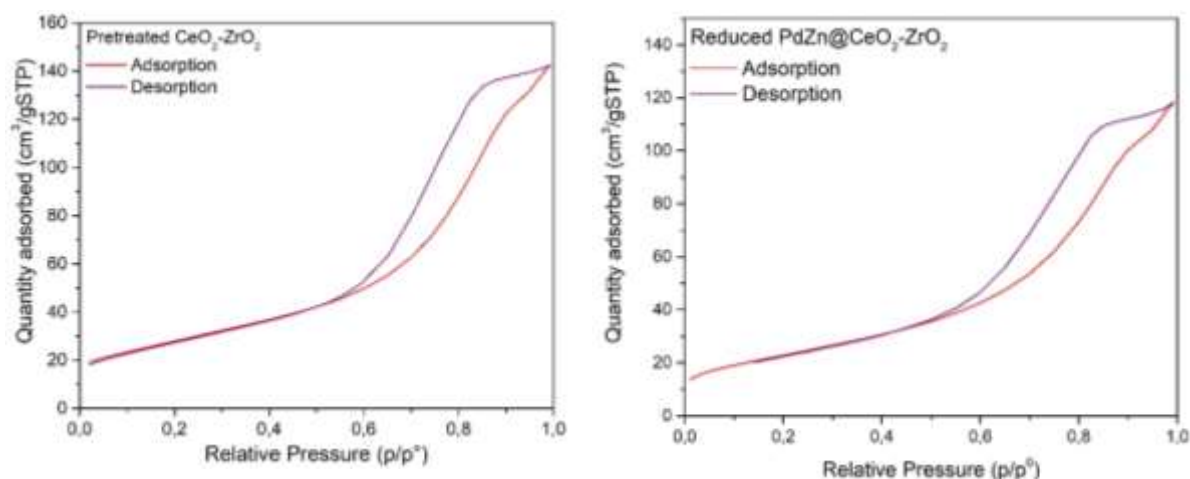


Figure S7. Isotherm linear plot of pretreated CeZrO_x (left) and reduced PdZn@CeZrO_x (right).

Table S3. Elemental analysis of the catalysts after grafting and after reduction.

Sample		Element	w%	Pd/Zn molar ratio
PdZn@CeZrO _x	Grafted	Pd	4.31	0.99
		Zn	2.68	
	Reduced	Pd	5.07	1
		Zn	3.10	
PdZn@CeO ₂	Grafted	Pd	2.34	0.98
		Zn	1.46	
	Reduced	Pd	4.85	0.96
		Zn	3.12	
PdZn@ZrO ₂	Grafted	Pd	4.50	1.02
		Zn	2.72	
	Reduced	Pd	5.26	1.06
		Zn	3.04	

Table S4. Average PdZn ratio obtained for the points sampled using EDX on: PdZn@CeO₂, PdZn@ZrO₂ and PdZn@CeZrO_x

Sample	Zn/Pd average ratio	Std deviation
PdZn@CeO ₂	0.6	0.2
PdZn@ZrO ₂	0.7	0.2

PdZn@CeOZrO _x	1.2	0.6
--------------------------	-----	-----

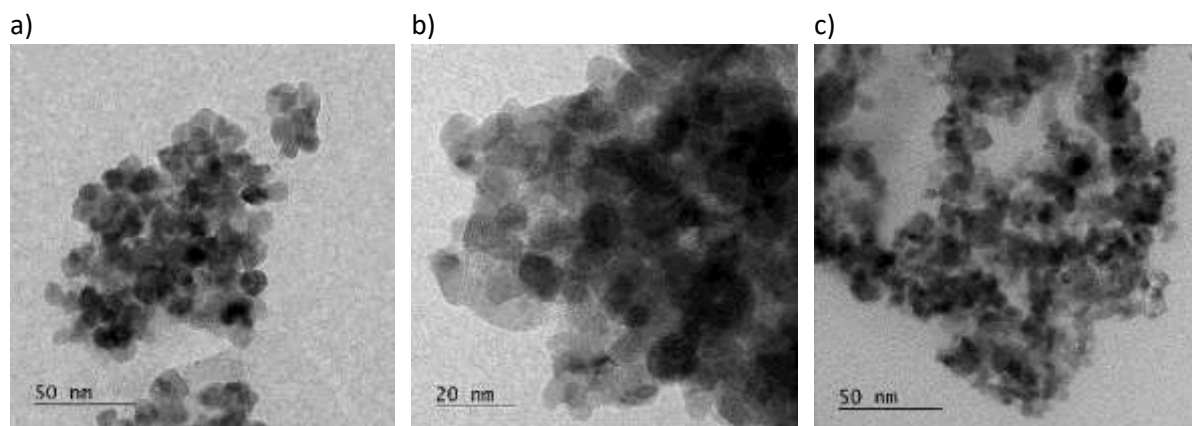


Figure S8. TEM images of the different systems: PdZn@CeZrO_x (a), PdZn@ZrO₂ (b), PdZn@CeO₂ (c)

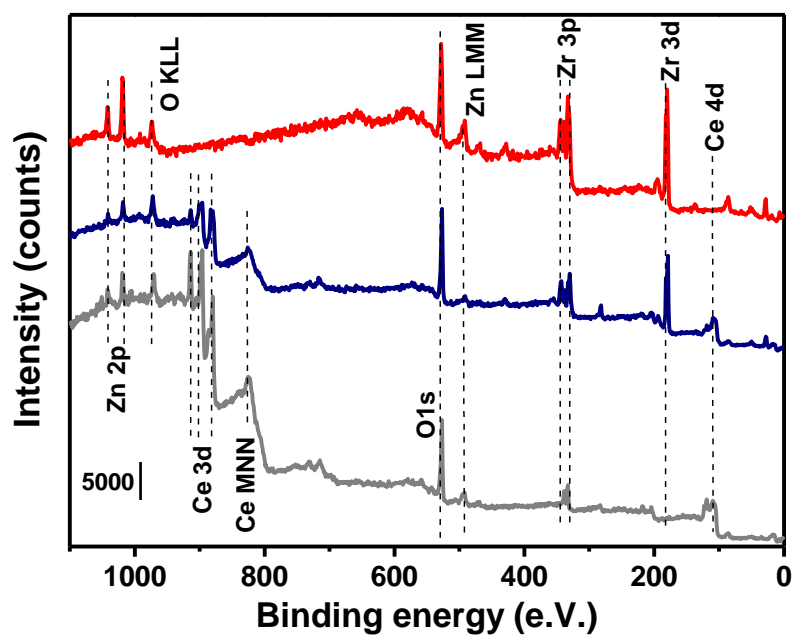


Figure S9. XPS survey spectra of PdZn@CeO₂ (gray), PdZn@CeZrO_x (blue) and PdZn@ZrO₂ (red).

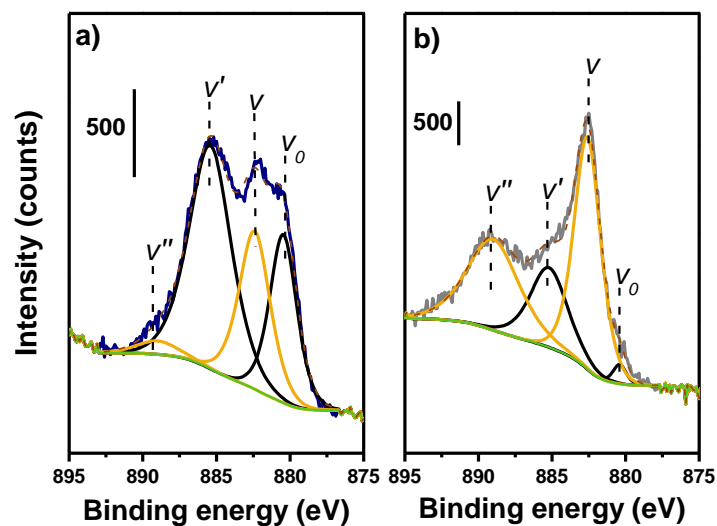


Figure S10 Best fit (dashed brown line) and XPS spectra of Ce 3d(5/2) region of a) PdZn@CeZrO_x (blue line) catalysts and b) PdZn@CeO₂ (grey line). v₀/v' and v/v'' indicates Ce³⁺ (black lines) and Ce⁴⁺ (yellow lines) electronic transitions, respectively. Shirley background is reported as green line.

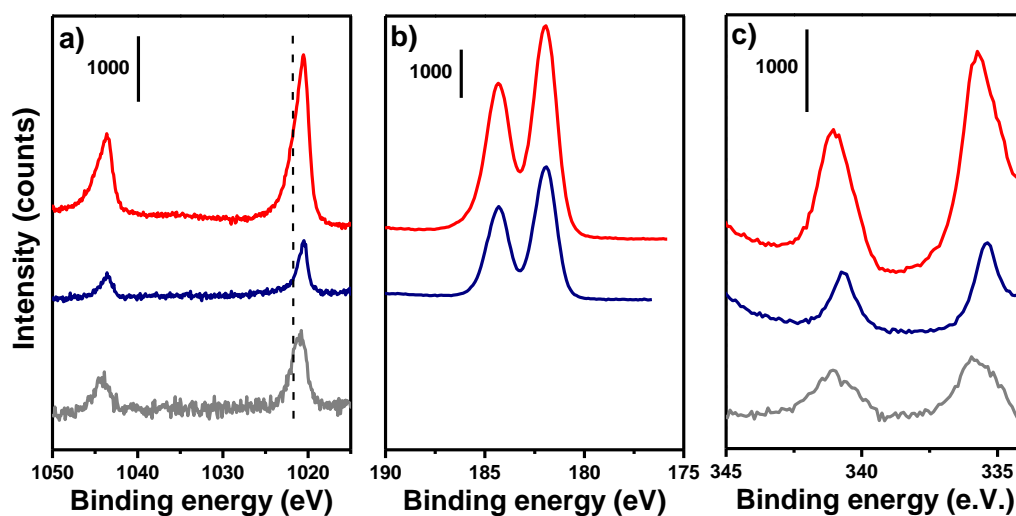


Figure S11. XPS spectra of a) Zn 2p, b) Zr 4p and c) Pd 3d regions of PdZn@CeO₂ (gray), PdZn@CeZrO_x (blue) and PdZn@ZrO₂ (red). Metallic/oxidic Zn 2p (1/2) BE is indicated by dashed line.

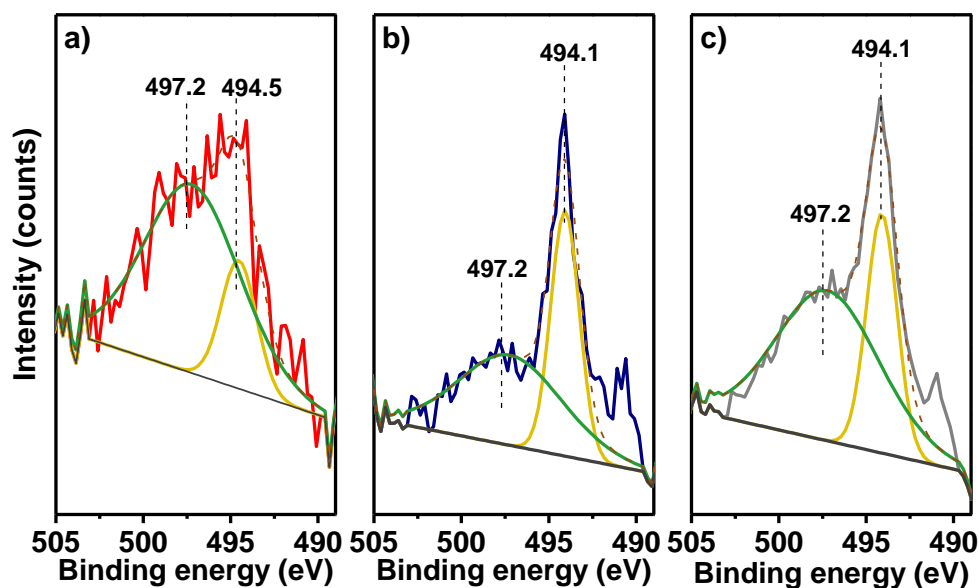


Figure S12. Fit (dashed brown line) and XPS spectra of Zn LMM auger line of a) PdZn@CeO₂ (red), b) PdZn@CeZrO_x (blue line) and c) PdZn@ZrO₂ (grey line) catalyst. Metallic/alloyed Zn and ZnO components are represented in yellow and green, respectively. Linear background is showed with grey line.

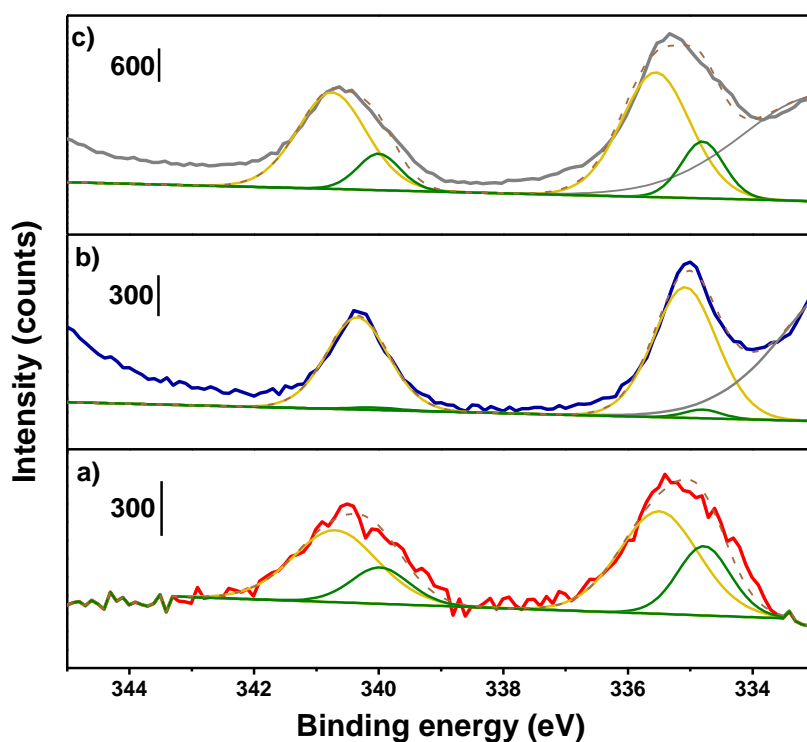


Figure S13. Detail of the Pd 3d best fit (brown dashed line) for a) PdZn@CeO₂ (red), b) PdZn@CeZrO_x (blue) and c) PdZn@ZrO₂ (gray). Component related to Pd metallic and Pd alloyed are represented in green and yellow, respectively. Band reported in gray line at lower Binding Energies represents Zr 3d 3/2 component which was considered for the fitting of PdZn@CeZrO_x and PdZn@ZrO₂.

Table S5. Full Width Half Maximum (FWHM) and Binding Energies (BE) resulting from the Pd 3d region fitting.

	PdZn@CeO ₂		PdZn@CeZrO _x		PdZn@ZrO ₂	
	FWHM (eV)	BE (eV)	FWHM (eV)	BE (eV)	FWHM (eV)	BE (eV)
Pd 3d (5/2) Pd metal	1.0	334.8	0.7	334.8	0.8	334.9
Pd 3d (5/2) PdZn alloy	1.5	335.6	1.2	335.1	1.3	335.8
Pd 3d (3/2) Pd metal	1.1	339.9	0.9	340.1	0.8	340.1
Pd 3d (3/2) PdZn alloy	1.6	340.9	1.2	340.3	1.3	341.1

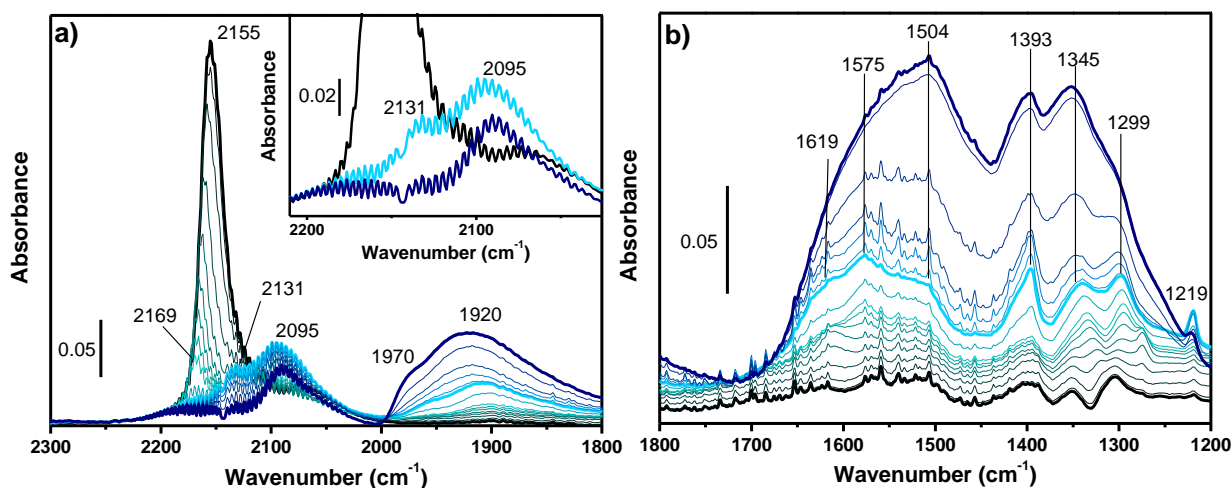


Figure S14. FTIR spectra of CO adsorbed over calcined PdZn@CeZrO_x during thermal evolution from LNT to RT. Carbonyls and carbonates main vibration regions are reported in panel a and b, respectively. Temperature increasing from LNT to RT is indicated by lines from black to light blue to blue.

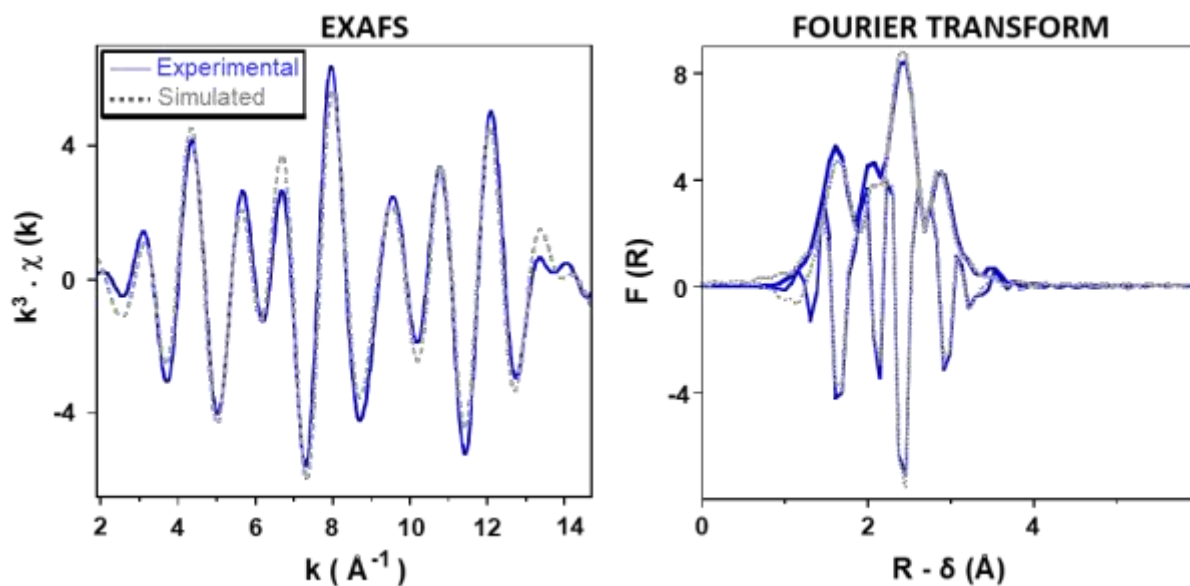


Figure S15. k^3 -weighted Zn K-edge EXAFS of reduced PdZn/CeZrOx in k -space (left) and Fourier transform (right, modulus and imaginary part). Solid blue line: From experimental data; dashed grey line: curve fit obtained with spherical wave theory.

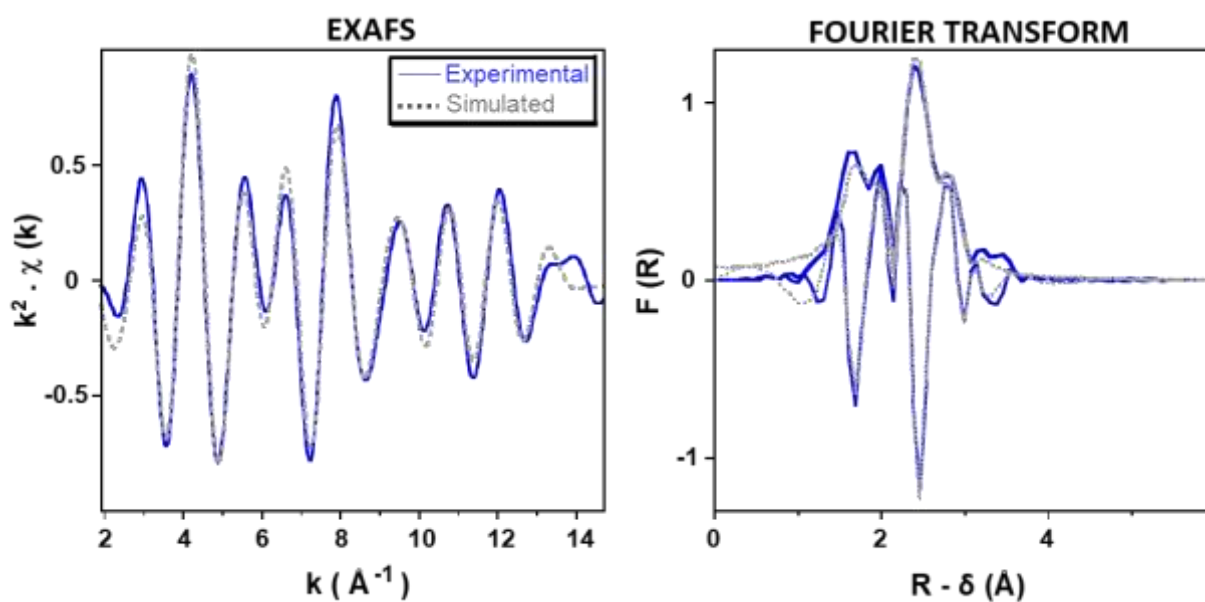


Figure S16. k^2 -weighted Zn K-edge EXAFS of reduced PdZn/CeZrOx in k -space (left) and Fourier transform (right, modulus and imaginary part). Solid blue line: From experimental data; dashed grey line: curve fit obtained with spherical wave theory.

Table S6. $k^2 \cdot \chi(k)$ EXAFS curve fit parameters for PdZn@CeZrOx after reduction.^(a)

Neighboring Atom of Zn	Number of Atoms N	Distance from Zn R(Å)	Debye-Waller Factor $\sigma^2(\text{\AA}^2)$
Zn-O^(b)	0.8(2)	1.98(2)	0.0014(7)
Zn-Pd^(c)	5.3(6)	2.60(1)	0.0103(10)
Zn--Zn^(c)	2.7 ^(d)	2.98(3)	0.0100(27)
Zn--Zn^(b)	2.4 ^(d)	3.24(3)	0.0082(32)

^(a) The errors on the last digit, generated by the EXAFS fitting program “RoundMidnight” are indicated in parentheses; Δk : [1.9 -14.7 Å⁻¹] - ΔR : [0.6-3.3 Å]; $S_0^2 = 0.92$; Fit residue: $\rho = 5.2\%$; Quality factor: $(\Delta\chi)^2/\nu = 3.01$, with $\nu = 12/24$. ^(b) From a ZnO phase, $\Delta E_{O1} = 1.3 \pm 2.6$ eV (fitted); ^(c) From a PdZn alloy phase, $\Delta E_{O2} = -1.1 \pm 1.3$ eV (fitted); ^(d) Shell constrained to a parameter above.

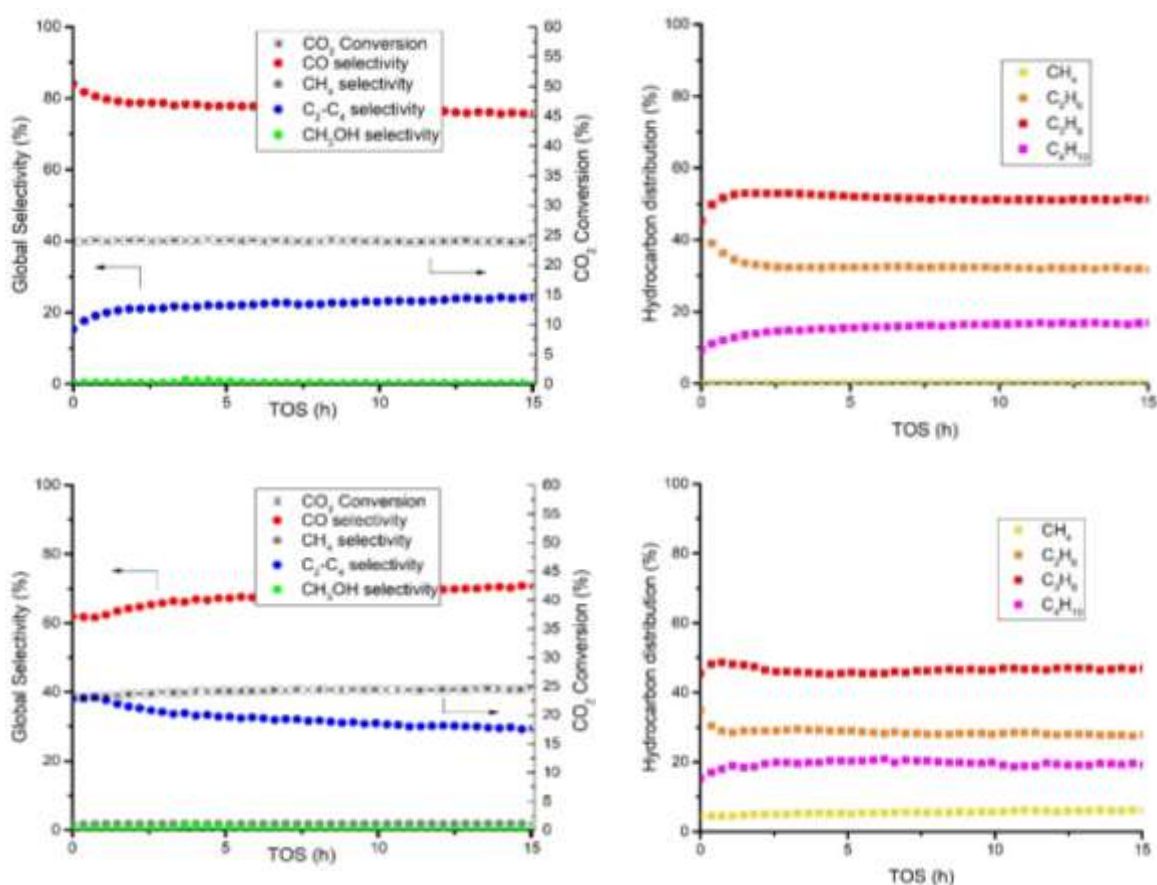


Figure S17. Conversion and product selectivity vs. time on stream (TOS) during the catalytic tests on PdZn@CeO₂ (top) and PdZn@ZrO₂ + SAPO-34 (bottom). Reaction conditions: 380 °C, 30 bar and 2000 ml/g/h.

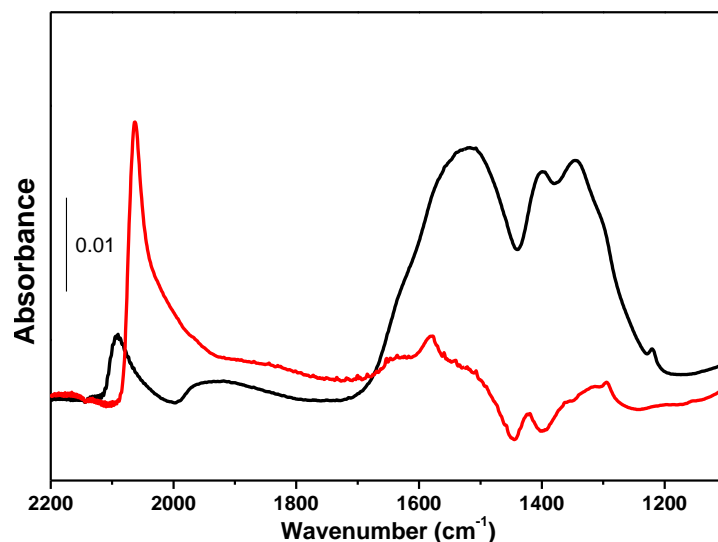
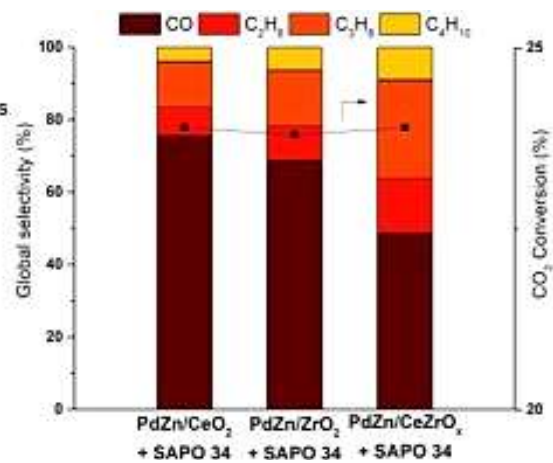
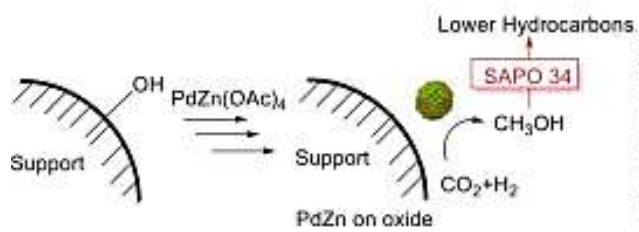


Figure S18. Detail of FTIR spectra measured after CO adsorption at RT over PdZn/CeZrO_x calcined (black line) and reduced (red line). Spectra are showed as difference by subtracting the activated catalyst spectra.

References

- [1] N.Y. Kozitsyna, S.E. Nefedov, F.M. Dolgushin, N.V. Cherkashina, M.N. Vargaftik, I.I. Moiseev, *Inorganica Chim. Acta* 359 (2006) 2072–2086.
- [2] T. Ishioka, Y. Shibata, M. Takahashi, I. Kanesaka, *Spectrochim. Acta. A. Mol. Biomol. Spectrosc.* 54 (1998) 1811–1818.
- [3] D.D. Kragten, R.A. van Santen, M.K. Crawford, W.D. Provine, J.J. Lerou, *Inorg. Chem.* 38 (1999) 331–339.
- [4] D.D. Kragten, R.A. Van Santen, M.K. Crawford, W.D. Provine, J.J. Lerou, *Inorg. Chem.* 38 (1999) 331–339.
- [5] T. Ishioka, Y. Shibata, M. Takahashi, I. Kanesaka, *Spectrochim. Acta - Part Mol. Biomol. Spectrosc.* 54 (1998) 1811–1818.
- [6] R. Knaanie, J. Šebek, M. Tsuge, N. Myllys, L. Khriachtchev, M. Räsänen, B. Albee, E.O. Potma, R.B. Gerber, *J. Phys. Chem. A* 120 (2016) 3380–3389.



TOC